ChemSusChem

Review
doi.org/10.1002/cssc.202201543

Chemistry Europe
European Chemical Societies Publishing

www.chemsuschem.org

Water Harvesting Strategies through Solar Steam Generator Systems

Casey Onggowarsito,[a] An Feng,[a] Shudi Mao,[a] Luong Ngoc Nguyen,[a] Jiangtao Xu,[b] and Qiang Fu*[a]

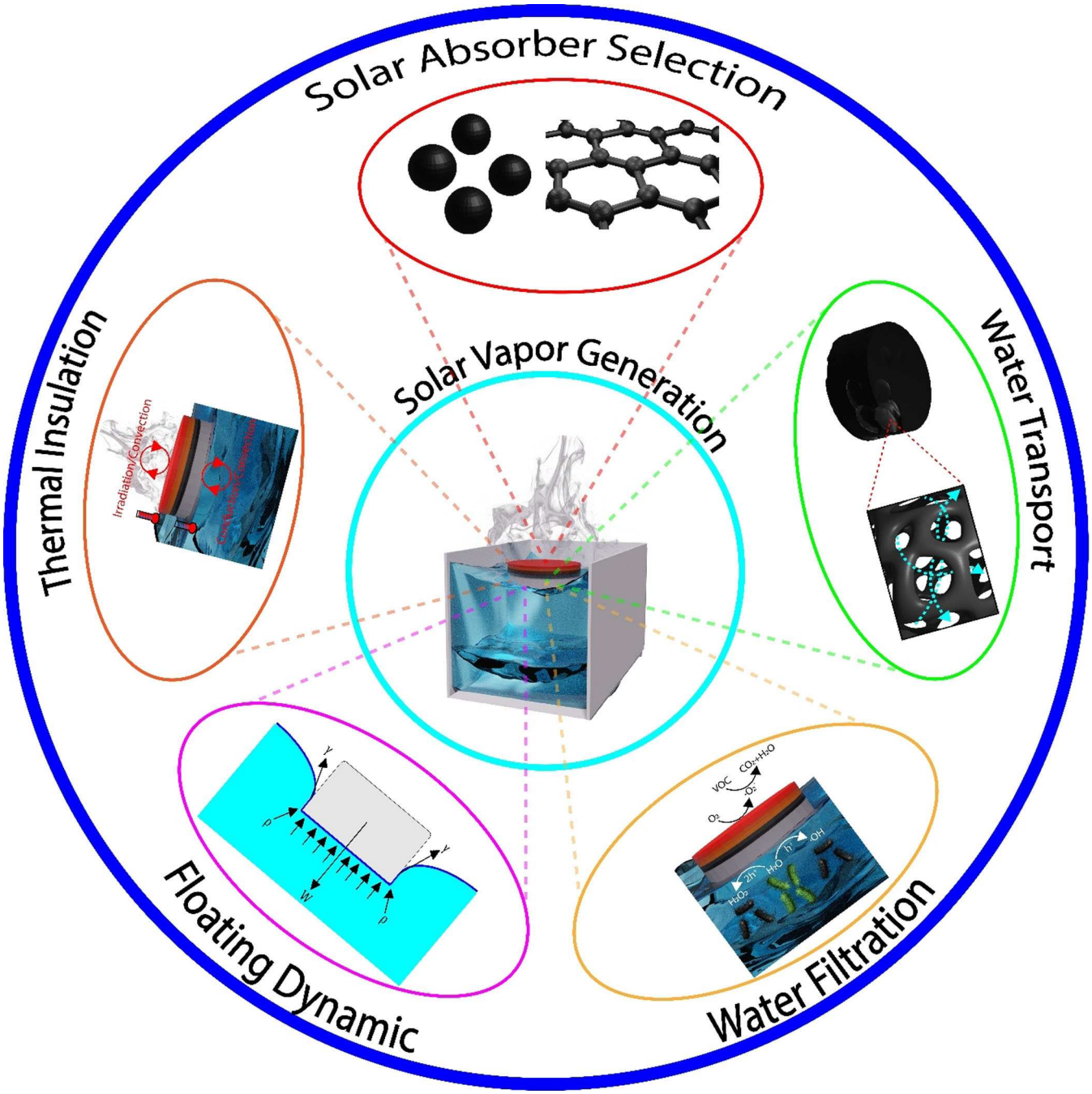

Solar steam generator (SSG) systems have attracted increasing attention, owing to its simple manufacturing, material abundance, cost-effectiveness, and environmentally friendly freshwater production. This system relies on photothermic materials and water absorbing substrates for a clean continuous distillation process. To optimize this process, there are factors that are needed to be considered such as selection of solar absorber and water absorbent materials, followed by micro/macro-structural system design for efficient water evaporation, floating, and filtration capability. In this contribution, we highlight the general interfacial SSG concept, review and compare recent progresses of different SSG systems, as well as discuss important factors on performance optimization. Furthermore, unaddressed challenges such as SSG's cost to performance ratio, filtration of untreatable micropollutants/microorganisms, and the need of standardization testing will be discussed to further advance future SSG studies.

1. Introduction

Water has played an imperative role which directly and indirectly impacted our daily life. Up to recently, there has been a high demand for freshwater resources with a projection of 55% increase by 2050 due to the increasing population and economic growth.[1] Over the past 100 years, water usage has increased by a factor of six and continuously grown 1% every year, supplying the demand of industrial/manufacturing, thermal power generation, agriculture, and domestic usage.[2] Apart from increasing water usage, population and economic growth have also introduced water pollution such as rising amount of wastewater from industrial and agricultural activities. Wastewater containing heavy metals, organics, fertilizer nitrogen and phosphorus pollutants can be detrimental towards human health.[3] This therefore further degrades our freshwater resource, resulting in an increase of demand. In addition, climate change[4] and the global pandemic situation of COVID-19 may have further worsened our current projected water demand.[5]

Currently, our on-going freshwater production relies on distillation/desalination systems such as thermal (multi-effect distillation, thermal vapor compression, and mechanical vapor compression), and membrane distillation (electrodialysis and reverse osmosis).[6] However, these systems contain high running cost (e.g., labor, energy, and real estate) and produce environmentally detrimental by-products such as high concentration of brine.[7] With the growing number of countries pledging for net-zero CO_2 emission,[8] a new efficient and greener approach known as solar steam generator (SSG) have recently shown to be a potential greener alternative.[9]

By harvesting solar energy with photothermic materials (such as plasmonic metals,[10] inorganic semiconductors,[11] conjugated polymer,[9b,12] and carbon-based materials),[13] SSG allows for continuous water generation with minimal amount of energy needed.[14] The conventional SSG, known as a volumetric SSG, was first proposed with the idea of uniformly dispersing photothermic materials throughout the water source (Scheme 1a). This thus caused the water source to be internally heated and water evaporating. However, this results in an inefficient solar-thermal conversion (ca. 30–45%) caused by thermal loss to the bulk water.[15] To further improve the efficiency, researchers have developed interfacial SSGs. In comparison with volumetric SSG, interfacial SSGs position photothermic materials near the water surface interface (Scheme 1b,c). A common strategy to achieve this is to utilize lightweight and floatable substrates such as foam or gel-based materials with an incorporated photothermic material. As a result, heat loss to bulk water is minimized and solar-to-vapor conversion efficiency is significantly increased to $>80\%$.[16]

In this Review, we highlighted recent development of interfacial SSG concerning variety of different factors including the selection of solar absorbers, water absorbent, and/or substrate material to be incorporated for efficient water evaporation, as well as micro/macro-structural system design for further optimization of water evaporation, floatation, and filtration purposes to generate freshwater. Furthermore, we discuss current challenges, such as material cost to performance and filtration of untreatable, viable but nonculturable (VBNC) bacteria, and provide insight into new performance benchmarking and internal SSG standardization testing for future research consideration.

[a] C. Onggowarsito, A. Feng, S. Mao, Dr. L. N. Nguyen, Dr. Q. Fu
Centre for Technology in Water and Wastewater
School of Civil and Environmental Engineering
University of Technology Sydney, 15 Broadway, Ultimo, NSW 2007 (Australia)
E-mail: qiang.fu@uts.edu.au
[b] Dr. J. Xu
Centre for Advanced Macromolecular Design, School of Chemical Engineering
UNSW Institution, Sydney, NSW 2052 (Australia)

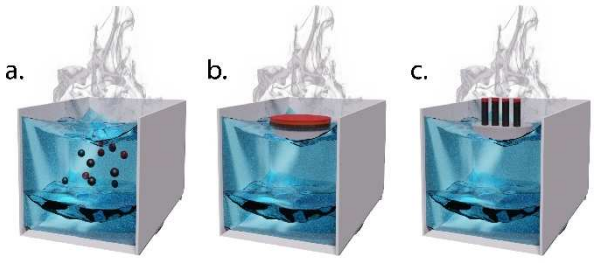

Scheme 1. Comparison between (a) volumetric, (b) 2D, and (c) 3D interfacial solar steam generators.

2. Solar Absorber Selection

SSG continuous supply of water generation relies on solar absorbers/photothermic materials ability to absorb light energy in the form of photon and converting its excess absorbed energy into heat for water evaporation.[17] However, it is unlikely for photothermic material to convert 100% solar energy into thermal energy. Factors such as the uneven distribution of solar energy throughout the light spectra (from UV to IR) and material surface light reflection are the main influence on inefficient solar-thermal conversion.[18] Therefore, solar-to-vapor conversion efficiency is quantitatively determined by water evaporation produced over the solar power given. This can be expressed as Equation (1):

$$\eta = \frac{Q_{vap}}{E_{solar}} \quad (1)$$

where Q_{vap} is the heat converted by the material and E_{solar} is the energy given by the solar irradiance. The generated heat (Q_{vap}) consists of water sensible heat as well as latent heat for it to change from liquid to vapor phase, which is shown by Equation (2):

$$Q_{vap} = \dot{m}C_p\Delta T + \dot{m}\Delta H_{vap} \quad (2)$$

where $\dot{m}$ is the evaporated water mass, C_p is the specific heat capacity of water (4.18 $J\,g^{-1}\,K^{-1}$), ΔT is the liquid temperature change, and ΔH_{vap} is the vapour latent enthalpy (2257 $kJ\,kg^{-1}$ at 100 °C). Therefore, the solar-to-vapor conversion efficiency can be expressed as follows:

$$\eta = \frac{\dot{m}(C_p\Delta T + \Delta H)}{c_{opt} I A \Delta t} \quad (3)$$

where A is the surface area of the SSG material, Δt is the evaporation time, c_{opt} is the optical concentration, and I is the solar irradiation (1 kW m^{-2}).[19]

To further increase SSG's solar-to-vapor conversion efficiency, a number of studies have incorporated photothermic materials with a wide light absorption range (UV to IR) capability into their system to harvest majority of the solar energy,[20] as well as utilized different design strategies in reducing potential light reflection on the material surface such as increasing surface roughness.[21]

2.1. Plasmonic metal nanoparticles

Localized surface-plasmon resonance (LSPR) is a phenomenon when free electrons are excited by light at a certain resonance wavelength oscillate near the particle's interface. Heat is produced when excited electrons are relaxed back to the ground state.[17b,22] As a result, plasmonic nanoparticles are able to have strong light absorption in the UV/Vis-NIR range, enabling an increase of incident light photon flux caused by the generated electric field.[22b,23] Despite this, plasmonic nanoparticles contain minor flaws such as complex manipulation, low thermal stability, and high cost compared to other photothermal materials.[17b,24]

Noble metal nanoparticles such as gold (Au) and silver (Ag) have been commonly used in SSG due to their strong light absorption (>70% solar energy harvesting).[25] For example, Fang et al. reported a SSG used layers of Ag/diatomite, filter paper, and polystyrene foam (Figure 1a). The Ag/diatomite composite contained a strong light absorbance of 250–2000 nm due to Ag nanoparticle LSPR and its frustule structure. As a result, the composite surface temperature was able to increase up to 44 °C in 30 min and generated an evaporation rate of 1.39 $kg\,m^{-2}h^{-1}$ with 92.2% efficiency under 1 sun.[10a] Another example of noble metal utilization is sandwich-like nanoplates demonstrated by Zhu et al. Au nanoparticles were coated on a prepared melamine sponge/reduced graphene oxide (rGO) nanoplates. This mixture was then further coated with rGO producing rGO/Au/rGO nanoplates and added on a hydrophilic substrate base as water transport. The wrinkled nanoplates with a broad light absorption of 400–1200 nm resulted in a maximum 75.5 °C surface temperature and a water evaporation rate of ~1.15 $kg\,m^{-2}h^{-1}$ with 63.35% efficiency under 1 sun.[10b]

Non-noble plasmonic semiconductor such as copper sulphate (CuS) is a common alternative to noble nanoparticles utilized in SSG due to its strong light absorption and relatively low cost.[26] For instance, Chen et al. incorporated CuS into their double cross-linking hydrogel-based SSG (CuS/CPM) consisting of polyacrylamide (PAAm) and carboxymethyl cellulose (CMC), which resulted in a relatively high 1.613 $kg\,m^{-2}h^{-1}$ with 79% efficiency under 1 sun (Figure 1c). The optimum CuS incorpo-

Casey Onggowarsito received his B.S. degree at the University of New South Wales. He is currently working towards his Ph.D. degree at the University of Technology Sydney under the supervision of Dr Qiang Fu. His current research focuses on synthesizing hydrogel-based materials for water purification.

Dr Qiang Fu completed his Ph.D. at Fudan University in 2009 before working as a Post-doctoral Fellow at the University of Melbourne. He was an ARC Super Science Fellow (2011–2014) and is currently an ARC Future Fellow (2018–2022). He joined the University of Technology Sydney in 2019. His research interests include functional polymer materials for energy and environmental applications, 2D materials, metal-organic frameworks, membranes for gas separation, macromolecular engineering, and controlled polymerizations.

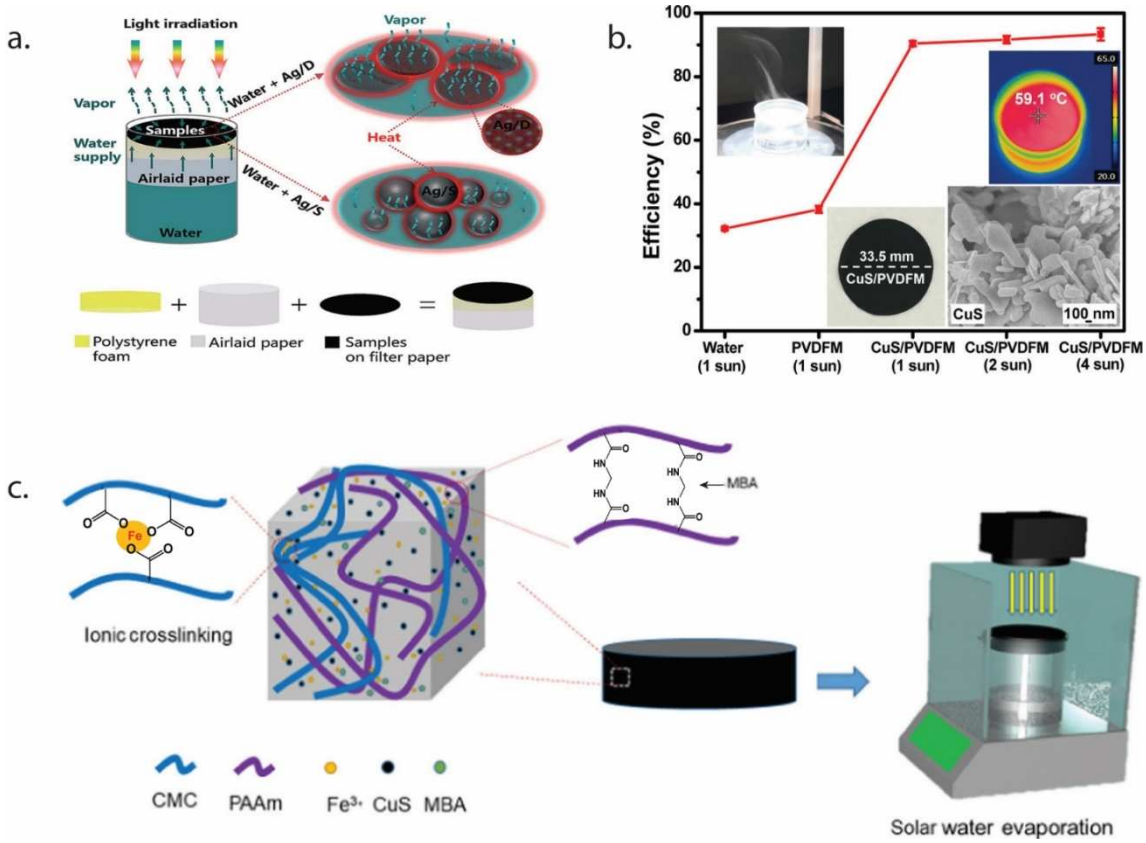

Figure 1. Schematic representation of noble metal plasmonic nanoparticle SSG designs: (a) Ag/diatomite composite. Reproduced with permission.[10a] Copyright 2017, The Royal Society of Chemistry. (b) Non-noble metal plasmonic nanoparticle CuS/PVDFM membrane. Reproduced with permission.[10d] Copyright 2018 American Chemical Society. (c) CuS/CPM hydrogel. Reproduced with permission.[10c] Copyright 2021 American Chemical Society.

ration increases the hydrogel light absorption capability at 250–2500 nm range. A further increase of CuS (>12 mg mL^{-1}) however reduced CuS/CPM light absorptance due to the increase of light reflectance. The incorporation of CuS (12 mg mL^{-1}) also allowed the hydrogel to achieved 47.2 °C surface temperature under 30 min at 1 sun.[10c] Additionally, Tao et al. reported a CuS/PVDFM membrane which relied on CuS nanoparticles LSPR to produce SSG (Figure 1b). The increase in light absorption between 300–2500 nm was caused and related to the concentration amount of CuS incorporation to the membrane. Interestingly, the SSG results showed that 12 mg-CuS/PVDFM was the optimal CuS concentration and therefore the most efficient membrane, generating 1.43 kg m^{-2} h^{-1} water evaporation rate with 90.4% efficiency under 1 sun. Moreover, 12 mg-CuS/PVDFM was able to heat its surface temperature up to 38.5 °C maximum at 1 sun.[10d] Besides CuS, a SSG made out of photothermal titanium nitride (TiN) nanoparticles reported by Guo and Yang layered on top of carbon wood water transport substrate (TBCF). TBCF SSG was shown to have a broad light absorbance of 400–2000 nm, owing to its rough, porous microstructure. Moreover, TBCF-1.5 (1.5 mg TiN deposition) with 10 mm substrate thickness was able to generate the highest water evaporation rate of 1.47 kg m^{-2} h^{-1} with 92.5% efficiency and a surface temperature maximum of ~45 °C under 1 sun.[27]

2.2. Inorganic semiconductor

Semiconducting materials contain band structures which are useful for photothermic property. This is due to the discrete atomic energy level in a solid is perturbed, causing electrons in each atoms occupying band levels. Semiconductors contain existing energy states of valence band where electrons fully occupy (maximum energy level) and conduction band where no electrons occupy (minimum energy level). In between these bands, no energy states exist which is known as forbidden band or band-gap (E_g).[28] Free charger carriers/electrons are excited by the oncoming light photon with an energy equal or greater to the E_g which leads to carrier transfer from valence to conduction band and resulting electron-hole pair. Excess charge carriers can then recombine through lattice heat generation or photon release.[29]

Wide E_g semiconductor is commonly used in optoelectronic applications due to its high stability and great absorption/emission in the UV region.[30] However, wide E_g semiconductors are unable to harvest solar energy throughout VIS-NIR region. Therefore, narrower E_g semiconductors are more favorable in photothermic application since it induces high carrier concentration flow.[31] High carrier concentration can lead to LSPR which increases the absorption range and results in an efficient solar-thermal conversion.[17b,32] There are different methods to

narrow semiconductor's E_g and one method is doping. Doping is the result of the introduction of impurities onto the semiconductor's crystal structure. This can be achieved by inducing the same (self-doping) or different (extrinsic doping) type of material. These impurities allow energy/impurities level to form between the valence and conduction band. Depending on the type of semiconductor doping (n-type/p-type), the fermi level will shift and narrowing the E_g close to either the valence or conduction band.[33] n-type carbon doped TiO_2 nanotube arrays and p-type iodine self-doped BiOI conducted by Kurian et al. and Zhang et al. respectively are some of the extrinsic and self-doping semiconductor examples. Based on these results, both materials show improvement in absorption range, covering UV/Vis region.[34] Similarly, oxygen vacancies caused by doping as shown by Tang et al. and Wang et al. of their cadmium stannate (CTO) and ZnO respectively, leads their materials to be p-type semiconductors and broadening the absorption range (UV-VIS). However, Tang et al. demonstrated that oxygen vacant CTO can be further doped with lanthanum (La), causing it to further broaden its absorption range to the IR region. This is because La doping causes the material to be more n-type semiconductor and therefore moving its fermi level close to the conduction band. The shift in fermi level causes the VIS range absorption capacity to reduce.[35]

Besides doping, another method to narrow the E_g is to introduce photosensitizer dyes, causing heterojunction formation. Heterojunction is usually formed due to E_g difference between two different semiconductor materials. A certain heterojunction formation can lead to an increase free charge carrier concentration and therefore broadening absorption capability.[36] For example, Sinha et al. showed light absorption increase of nanostructure ZnO with the addition of curcumin dye, broadening the absorption spectrum from UV to VIS region.[37] Furthermore, similar result had shown in Yarahmadi and Sharifinia's ZnO, by adding variety of photosensitizer dyes including Co, Ni, and Cu phthalocyanines (Pc).[38]

In addition, semiconductor light absorption can be further improved by incorporating plasmonic nanoparticles due to its LSPR generation, as mentioned previously. There are different mechanisms for plasmonic energy transfer to occur, such as hot electron injection, light trapping/scattering, and plasmon-induced resonance energy transfer (PIRET).[28,39] Hot electron injection is the resultant of nonradiative small decaying plasmonic nanoparticles (<20 nm) free charge carrier transfer to the semiconductor's conduction band. The charge transfer is caused due to the excited charge energy produced by the absorbed photon exceeds the semiconductor's Schottky barrier. Ratchford et al. demonstrated hot electron injected gold nanoparticles to TiO_2 caused an increase in light absorption, broadening it to the visible range.[40] Unlike hot electron injection, both light trapping and PIRET mechanism uses radiative/dipole-dipole interaction. Light trapping is done by scattering light with a large plasmonic nanoparticles (>50 nm), on to the semiconductor's interface. Surface plasmon resonance (SPR) is then generated due to the scattered light which increases absorption.[41] For example, Morawiec et al. observed an absorption enhancement in their hydrogenated amorphous silicon (a-Si:H) thin film solar cell system due to the light trapping from the incorporation of silver nanoparticles.[42] Besides light scattering, high absorption cross-section plasmonic nanoparticles can be used as light concentrator.[43] PIRET utilizes this feature to increase free charge carriers generated in the semiconductor. The mechanism behind this is based on nanoparticle's LSPR dipole-dipole interaction with semiconductor's LSPR when exposed to light, generating electron-hole formation. Furthermore, the incident light intensity no longer acts as a limiting factor of semiconductor charge carrier generation. Cushing et al. proved the increase in light absorption by developing an Ag@TiO_2 PIRET generating system. Interestingly, they selected either PIRET or hot electron injection, as well as both phenomena to occur in their system by adjusting the material content. Moreover, they found that only PIRET will occur if there are overlaps between the plasmonic particles and semiconductor LSPR. As LSPR overlapping occur less, the system will favor more towards hot electron injection.[44]

Titanium oxide (TiO_2) is a commonly used inorganic semiconductor in SSG due to its low cost and toxicity, great stability, and has been extensively studied for its photocatalytic activity.[45] Black TiO_2 ($BTiO_2$) film developed by Zada et al. is one of the examples of TiO_2 SSG (Figure 2a). $BTiO_2$ was obtained through sol-gel process, calcination of produced TiO_2, as well as mixing with polyvinylidene fluoride (PVDF) film formation. $BTiO_2$ was found to have a strong light absorption (250–2500 nm) due to its black colored surface when compared with white TiO_2 as well as its particle random size distribution (100–800 nm) which caused multiple light reflection and scattering. Consequently, this SSG was able to heat its surface temperature up to 45.4 °C in 1 h and generate water evaporation rate of 1.16 $kg\,m^{-2}\,h^{-1}$ with 77.14% solar efficiency under 1 sun.[11a] Similarly, Kim et al. altered TiO_2 nanorods (TNRs) from TiO_2 film (TF) grown on glassy carbon foam (CF) was able to produce a high 2.23 $kg\,m^{-2}\,h^{-1}$ water evaporation rate with 67.1% efficiency under 1 sun (Figure 2b). This is due to its high surface roughness compared to TF/CF caused by the nanorod morphology which provided the enhancement of evaporation surface area. Furthermore, TNRs/CF foam pores allowed sunlight trapping/scattering resulting in a strong light absorption between 200–2500 nm. Though, TNRs/CF showed a lower surface temperature (41.4 °C) compared to TF/CF (46.4 °C) due to the high-water presence.[11b] Besides TiO_2, iron oxide (Fe_3O_4) is another inorganic semiconductor which is commonly used in SSG application due to its narrow band gap, wide solar absorption, low cost, good biocompatibility and low toxicity.[46] An example of this is demonstrated by Song et al. developed a Fe_3O_4/PVA (polyvinyl alcohol) coated wood (Fe-D-Wood) system (Figure 2c). The hydrophobic Fe_3O_4/PVA deposition layer provides additional surface roughness which allows for strong light absorption up to 97% between UV-NIR. As a result, Fe-D-Wood was able to generate a surface temperature of ~58 °C under 1 sun which is much higher compared to natural wood itself (ca. 34 °C). Moreover, the Fe-D-Wood system managed to achieve 1.3 $kg\,m^{-2}\,h^{-1}$ water evaporation rate with 73% efficiency.[11c] Additionally, MXene materials such as titanium carbide ($Ti_3C_2T_x$)

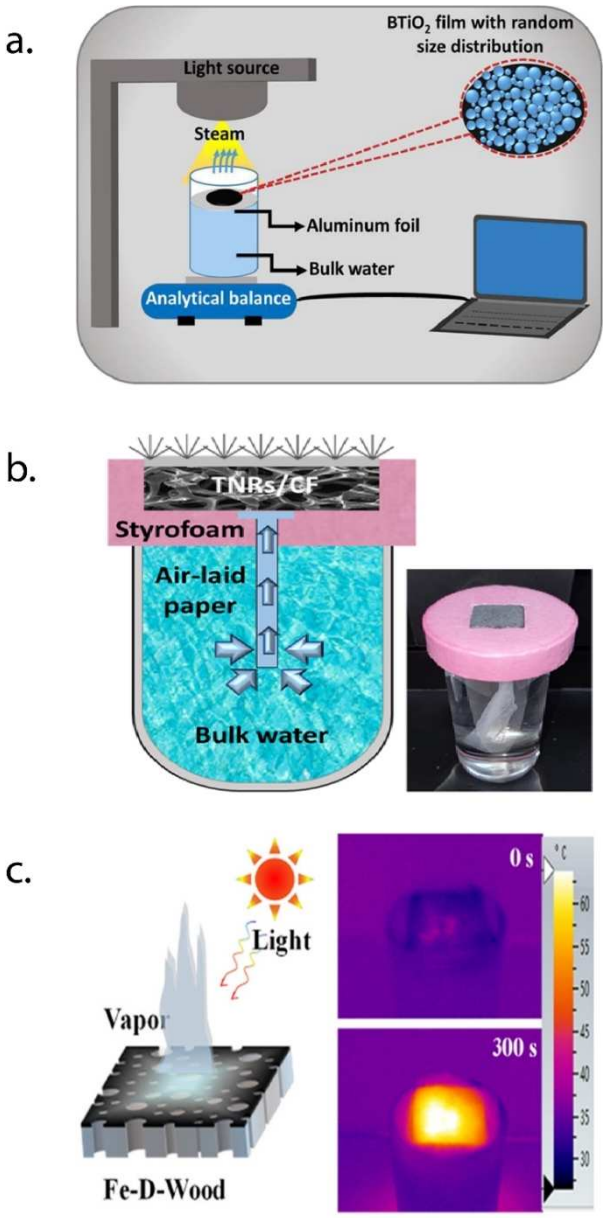

Figure 2. Schematic representation of inorganic semiconductor SSG applications: (a) $BTiO_2$ film. Reproduced with permission.[11a] Copyright 2020, Elsevier Ltd. (b) TiO_2 nanorods. Reproduced with permission.[11b] Copyright 2021, American Chemical Society. (c) Fe_3O_4/PVA Fe–D-Wood. Reproduced with permission.[11c] Copyright 2021, Elsevier B.V.

and niobium carbide (Nb_2CT_x) can be another alternative towards metal oxides shown in previous examples. Ai et al. recently developed a hierarchical binary gel (HBG) consisting of 2-layer chitosan-based gel with Ti_3C_2 MXene on the top light absorbing layer and montmorillonite (MMT) on the water absorbing/thermal insulating bottom layer. Ti_3C_2 gel demonstrated 94% absorption efficiency between 400–2500 nm. Furthermore, Ti_3C_2 gel was able to generate a stable surface temperature of 51 °C under 1 sun. Under optimal Ti_3C_2 loading (5 wt%), HBG was able to produce 1.36 kg m^{-2} h^{-1} water evaporation rate with 93.7% efficiency.[47] Another example of MXene utilization can be seen in Xia et al. developed copper selenide ($Cu_{2-x}Se$)/Nb_2CT_x nanocomposites. The combination of semiconductor $Cu_{2-x}Se$ with Nb_2CT_x MXene nanosheets allow the nanocomposites to achieve broad light absorption ability between 250–1400 nm. Moreover, $Cu_{2-x}Se$/Nb_2CT_x nanocomposites managed to produce high thermal generation of 47.1 °C under 1 sun. With the help of hydrophilic and low thermal conductive glass microfiber filters, this system was able to generate 1.2 kg m^{-2} h^{-1} simulated seawater evaporation under 1 sun irradiation for 30 min.[48]

2.3. Conjugated polymers

Conjugated polymers are commonly used as photothermal applications such as for biomedical photothermal therapy. Owing to their great optical property caused by its π-π* transition when exposed to light. Moreover, conjugated polymers are low-cost and can be easily engineered.[49] Similar to semiconductor, the absorption property of conjugated polymer can be expanded by narrowing its E_g through coupling electron donor and acceptor polymers. However, this leads to compensating the material thermal stability. Despite this, there are methods to prevent the reduction of thermal stability such as shown by Griffini et al. through the incorporation of either diblock copolymer compatibilizer, fullerene attached diblock, and thermally crosslinked donor or acceptor polymer.[50]

Polypyrrole (PPy) is a popular material used in SSG application. An example of PPy utilization can be seen in PVA hierarchically nanostructured gel (HNG) developed by Zhao et al. This gel was able to have a strong light absorption between 400–2500 nm due to the incorporation of PPy. Moreover, the strong light absorption allowed the gel to reach a maximum surface temperature of 41.3 °C and was able to generate an impressive 3.2 kg m^{-2} h^{-1} with 94% efficiency under 1 sun.[9b] Additionally, Zhu et al. blended PPy and pyridine-based aerogels (PCMPAs) showed similar results. The included PPy allowed PCMPAs gel to have broad light absorption of 400–2500 nm compared to regular PCMPAs (400–800 nm) (Figure 3a). The resultant PCMPAs-PPy was able to achieve a higher surface temperature of 42.2 °C compared to PCMPAs 35.4 °C. As a result, PCMPAs-PPy also generated higher water evaporation rate of 1.4304 kg m^{-2} h^{-1} with 80% efficiency compared to PCMPAs 0.8838 kg m^{-2} h^{-1} evaporation rate with 44% efficiency under 1 sun.[12a] Another example of PPy usage can be seen in the PVA/PPy hydrogel membrane. In this study, Shi et al. investigated different types of topology surface designs such as flat surface, cone, cylinder, and micro-tree structured. These hydrogels showed light absorption above 90% at 250–2500 nm. The thermal result showed that flat surface hydrogel had the highest surface temperature compared to micro structured surface gels. However, Shi et al. found that microstructured gels had higher heat consumption than flat surface gel through gel-air interface, as well as minimized heat dissipation to the gel underneath. Among these microstructured gels, the micro-tree structure could retain the highest overall surface temperature of about 28 °C under 1 sun,

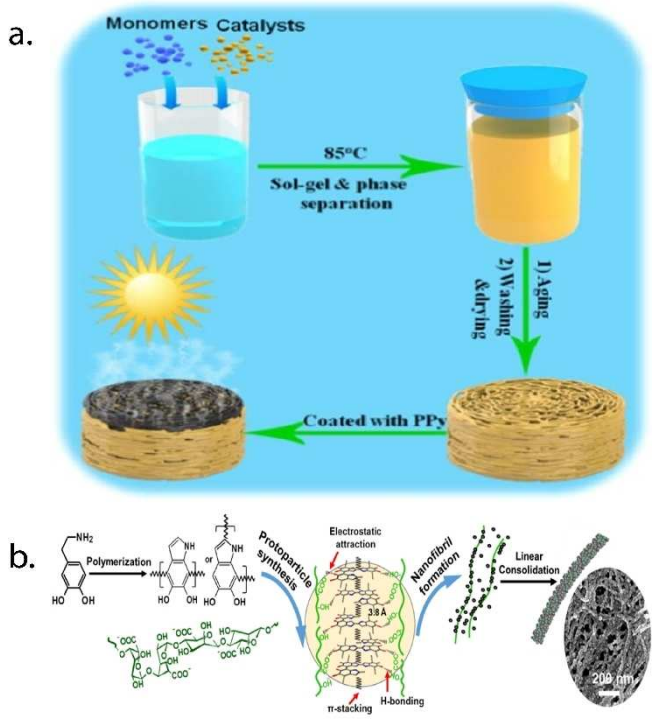

Figure 3. (a) Schematic representation of the synthesis method of PCAMPAs-PPy gel. Reproduced with permission.[12a] Copyright 2020, Elsevier Ltd. (b) Synthesis and SEM diagram of PDA nanofibril gel. Reproduced with permission.[12b] Copyright 2018, Elsevier Ltd.

owing to higher surface exposure to light obtained by the cone branches. As a result, the micro-tree structure gel produced 3.64 $kg\,m^{-2}\,h^{-1}$ water evaporation rate with roughly 96% efficiency.[51]

Polydopamine (PDA) is another example of conjugated polymer which is known to be used as synthetic melanin and also widely used in biomedical applications due to their broad absorption range, radical scavenging ability, and antioxidant activity.[52] In terms of SSG, Zong et al. managed to develop PDA nanofibrils SSG consisted of PDA and alginate on top of Ca^{2+}-alginate aerogel (Figure 3b). The alginate appliance transformed the PDA nanoparticle into PDA nanofibril structure. Moreover, alginate increased the π conjugation content for PDA nanofibrils which led to an increase of light absorption between 200–800 nm compared to PDA nanoparticles. In addition to conjugation content, the granular surface structure of PDA helped reduce light reflection which contributed to the strong light absorption. This resulted the PDA nanofibrils surface temperature to heat up to 45 °C and generated 1.72 $kg\,m^{-2}\,h^{-1}$ with approximately 90% efficiency under 1 sun.[12b]

2.4. Carbon-based materials

A low cost and highly abundant carbon derived materials are one of the most frequently utilized photothermal materials. Many types of carbon materials contain sp^2 and/or sp^3 hybridization structure which allows them to have high absorption of light and thermal conductivity from electron conduction and lattice vibration. Since σ shell absorbs only at UV region, an increase in sp^2 and π electron density would lead to an increase in light absorption.[15b,53] However, this is not necessarily true for thermal conductivity as shown by the results of nonequilibrium molecular dynamic (NEMD) simulation on nanodiamond thermal conductivity study from Matsubara and co-workers. In this study, the nanodiamond was sandwiched between two copper (Cu) crystal blocks to introduce gradual heat exposure. They found that nanodiamond thermal conductivity is dependent on its chemical structure of the ratio between sp^2 and sp^3. The thermal conductivity of nanodiamond was shown to decrease with an increasing sp^2 structure ratio to sp^3. This highlights the effectiveness of sp^3 bond lattice vibration heat transfer in comparison to sp^2 bond.[54] Despite this, carbon-based materials contain some disadvantages such as having limited recyclability. For example, graphene and graphite materials are vulnerable to pollutants and salt contamination.[55] Moreover, carbon-based nanocolloids are known to be potentially cytotoxic and environmentally unfriendly.[56]

Graphene-based materials such as vertically aligned reduced graphene oxide (VrGO) foam reported by Li et al. are one of the most common photothermal materials used in SSG. In this example, VrGO was produced through unidirectionally freezing the GO suspension from its bottom. As a result, VrGO consisted of vertical pore channels for upward transport of water for an efficient SSG (Figure 4a). In addition, VrGO demonstrated a strong light absorption throughout 220–2500 nm and produced a surface temperature of 35.5 °C under 1 sun. Moreover, the decreased of vaporization enthalpy from dynamic compression resulted in VrGO (with 47.1% compression strain) producing a water evaporation rate of 3.39 $kg\,m^{-2}\,h^{-1}$ with 104.1% apparent efficiency under 1 sun.[13a]

Carbon nanotubes (CNTs) is another common carbon derived materials used in SSG besides graphene-based materials. Wang et al. managed to combine rGO with multiwalled CNTs (MWCNTs) to produce a flexible SSG membrane (Figure 4c). For this study, the SSG performance was highly influence by the material surface roughness. This is because surface roughness affects the material optical property such as its light absorption, reflection, and transmission. G-88C membrane was resulted to have the highest surface roughness compared to other rGO-MWCNTs membranes. As a result, G-88 C was able to generate the highest surface temperature (77.6 ± 2.2 °C in 30 min under 1 sun) induced by its minimum light reflection and transmission between 300–2500 nm. This lead G-88C to produce 1.22 $kg\,m^{-2}\,h^{-1}$ water evaporation rate with 80.4% efficiency.[13b]

In addition, biomass-derived carbon materials have been widely utilized as a low-cost renewable resource alternative.[57] Recently, Liu et al. was able to construct a 3D SSG application using carbonized pomelo peels wrapped in polyethylene foam (CPP). The resultant CPP demonstrated great light absorption (92%) with minimal transmittance and reflectance between 250–2500 nm. As for SSG performance, CPP containing three

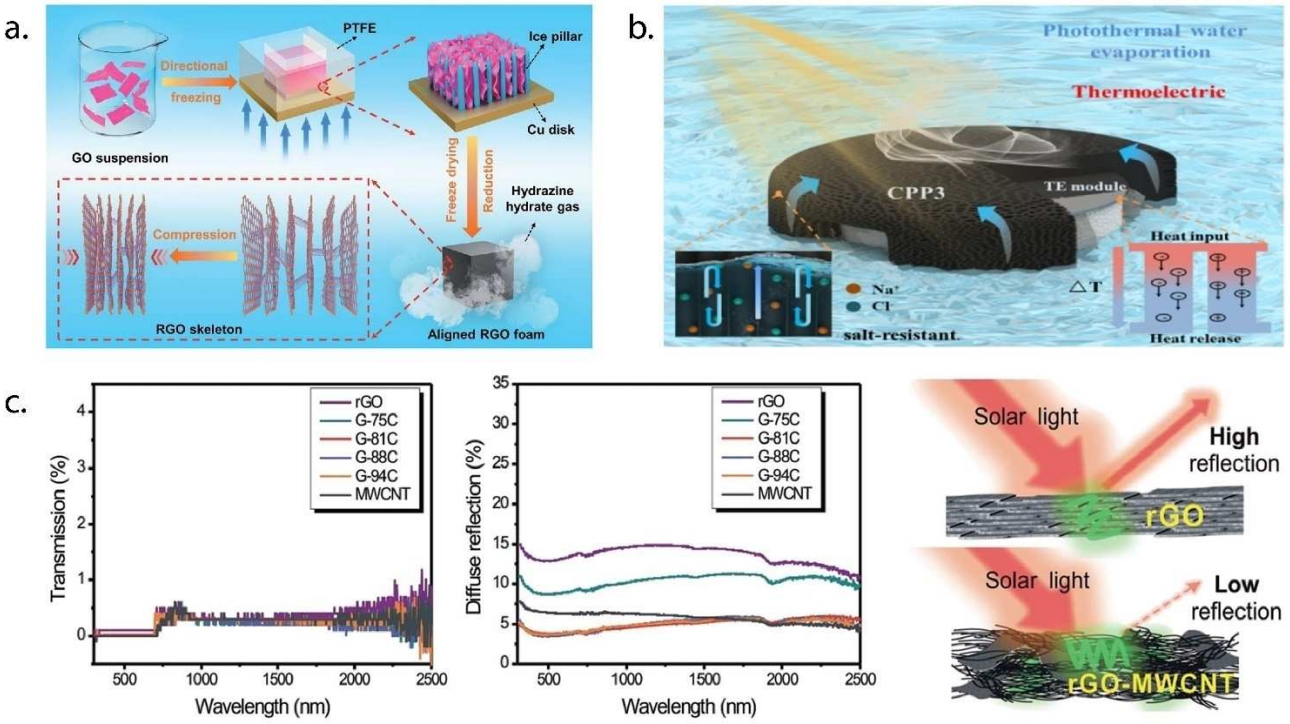

Figure 4. (a) Schematic diagram of VrGO foam fabrication. Reproduced with permission.[13a] Copyright 2021, The Royal Society of Chemistry. (b) Schematic illustration of CPP foam with three waterways channel (CPP3). Reproduced with permission.[13c] Copyright 2021, American Chemical Society. (c) Light absorption/reflection performance of rGO-MWCNTs membrane by UV/Vis-NIR spectroscopy. Reproduced with permission.[13b] Copyright 2018, The Royal Society of Chemistry.

waterways channel (CPP3) was shown to be the best (Figure 4b), generating 1.37 $kg\,m^{-2}\,h^{-1}$ water evaporation rate with 93.7% efficiency and thermal generation of 46.6 °C at the surface.[13c] Furthermore, Fang et al. utilized carbonized lotus seedpods as their SSG material. This material was able to have 98–99% light absorption between 250–2000 nm. For its heat generation ability, the carbonized lotus seedpods demonstrated a maximum surface temperature of 80 °C and 44.8 °C during SSG testing under one sun. As a result, this SSG system managed to produce 1.30 $kg\,m^{-2}\,h^{-1}$ with 86.5% efficiency under 1 sun.[58]

Table 1. Summary of different photothermal material types' advantages and disadvantages.

Photothermal Material Type	Advantages	Disadvantages
Plasmonic metal nanoparticles	Broad light absorption	Complex manipulation Low thermal stability High production cost
Inorganic semiconductor	Strong light absorption High thermal stability Low production cost Low toxicity	Narrow light absorption Complex manipulation
Conjugated polymers	Low production cost Easily synthesize Strong light absorption	Low thermal stability
Carbon-based material	Strong light absorption Low production cost Abundant Easy production	Limited recyclability Cytotoxic

2.5. Photothermal materials comparison

In this section, we have highlighted the advantages and disadvantages of each photothermal materials, as summarized in Table 1. Many recent review articles shared similar discussion on the advantages of each photothermal material types provide. However, many of these reviews have neglected the disadvantages of each photothermal materials bring.[59] Additionally, a series of SSG studies between 2017 to 2022 were gathered and categorized based on the type of photothermal material used, to compare both water evaporation performance and efficiency difference (Table 2).

Many studies have used carbon-based photothermal materials (Figure 5). This may be due to the abundance, low-cost, and noncomplex production of carbon-based materials. Moreover, carbon-based SSGs contain high average water evaporation rate and solar-to-vapor conversion efficiency, being slightly lower than for conjugated polymer SSGs. Parenthetically, a carbonized cattail SSG developed by Zhang et al. showed >100% apparent efficiency, owing to their system's structural design in obtaining back its energy loss to the environment (see below; Figure 7c).[60] In addition, carbon-based SSG have the highest result variance in evaporation rate (ranging from about 0.9–4.2 $kg\,m^{-2}\,h^{-1}$), as well as efficiency (ca. 68–105%). The high evaporation rate result variance can also be seen in

Table 2. Summary of different photothermal materials and SSG performances in recent studies (2017–2022).

Solar Steam Generator (SSG)	Year	Photothermal Materials (PTM)	Water Evaporation Rate Under 1 Sun [kg m^{-2} h^{-1}]	Efficiency [%]	Maximum Surface Temperature [°C]	Ref.
Three-level pore structure hydrogels (TLPSHs) (rGO/PVA)	2022	Carbon-based	1.65	75	45.2	[64]
Carbonized cattail (CCT)	2021	Carbon-based	4.12	105.8	30.9	[60a]
Bryophytes/green moss	2021	Carbon-based	2.61	69	35	[65]
Hydrogel-based ultrathin membrane (HUM) (carbon black/PVA)	2021	Carbon-based	2.4	80	37	[9a]
PVA/SLS-CNT hydrogel (PSCH)	2021	Carbon-based	2.09	80.4	47.1	[66]
Nanofibrous hydrogel-rGO membrane (NHrG)	2021	Carbon-based	1.85	95.4	40	[67]
PT-1-1 (PMAAc/TMEDA) hydrogel with black carbon-based oily ink	2021	Carbon-based	1.5	91	40	[68]
Carbonized corn straw (CSMC)	2021	Carbon-based	1.422	89.3	54.4	[69]
Carbonized pomelo peel (CPP)	2021	Carbon-based	1.37	93.7	46.6	[13c]
Interpenetrating polymer networks gel (IPNG) (PVA-activated carbon/PSS)	2020	Carbon-based	3.86	92	33	[9c]
Molybdenum carbide/carbon-based chitosan hydrogel (MoCC-CH)	2020	Carbon-based	2.19	96.15	40.5	[70]
Carbonized rice husk biochar (RHB)	2020	Carbon-based	1.77	94	88.5	[71]
Carbonized corn straw	2020	Carbon-based	1.497	86	40.7	[72]
Carbonized daikon	2019	Carbon-based	1.57	85.9	32.6	[73]
Chitosan/reduced graphene oxide blank hollow spacer fabric (BHSF)	2019	Carbon-based	1.4352	86	45.4	[74]
Span80/isodecyl acrylate (IA)/divinylbenzene (DVB) gel emulsion	2019	Carbon-based	1.27	90.3	42.3	[75]
Candle soot nanoparticle-decorated wood	2019	Carbon-based	0.95	67.9	34.7	[76]
Capillarity facilitated water transport hydrogel (CTH) (PVA/rGO)	2018	Carbon-based	2.5	95	32	[77]
Cellulose/carbon black coated cotton	2018	Carbon-based	1.62	96	31.6	[60b]
Carbonized lotus seapod	2018	Carbon-based	1.3	86.5	44.8	[58]
rGO-multi-walled carbon nanotube (MWCNT) membrane	2017	Carbon-based	1.22	80.4	47	[13b]
Poly(N-phenylglycine)/wood solar evaporator	2022	Conjugated Polymer	1.64	90.4	54	[78]
PVA/PPy gel membrane	2021	Conjugated Polymer	3.64	96	28	[51]
DPP-TPA/PVA covalent organic framework hierarchical structure (COFHS)	2021	Conjugated Polymer	2.5	93.2	49.5	[79]
Chitosan/PAAm/PPy hydrogel	2021	Conjugated Polymer	2.41	92	40	[80]
PPy-compounded air laid paper (PPy-AP)	2021	Conjugated Polymer	2	93.5	36.4	[81]
PPy/$FeCl_3$ coated melamine foam	2020	Conjugated Polymer	2	90	65.7	[82]
Pyridine-based conjugated microporous polymer aerogel (PCMPA)-PPy	2020	Conjugated Polymer	1.4304	80	42.2	[12a]
PPy coated-porous ionic polymer(PIP)	2020	Conjugated Polymer	1.55	89.8	40.2	[83]
PPy/$FeCl_3$ coated pomelo peel	2020	Conjugated Polymer	1.22	76.61	50.8	[84]
h-LAH hydrogel (PVA-chitosan/PPy)	2019	Conjugated Polymer	3.6	92	33.4	[85]
PPy coated porous foam-based aromatic polymer (PDVB-PS)	2019	Conjugated Polymer	1.3986	87.6	44.6	[86]
Monolithic PPy sponge	2019	Conjugated Polymer	1.447	84.72	44.4	[87]
PVA/PPy hierarchically nanostructured gel (HNG)	2018	Conjugated Polymer	3.2	94	41.3	[9b]
Polydopamine nanofibrils/polystyrene foam	2018	Conjugated Polymer	1.72	90	45	[12b]
PPy coated cotton/polystyrene foam	2018	Conjugated Polymer	1.2	82.4	33.1	[88]
Fe^{3+}-TA@eggplant aerogel	2022	Plasmonic Metal Nanoparticle	1.61	98.01	48.2	[89]
Silicon (Si) nanowire/polyethylene foam	2022	Plasmonic Metal Nanoparticle	1.12	72.8	33.9	[90]
Agar hydrogel (AHG)/Prussian blue (PB)-cellulose nanofiber (CNF)	2021	Plasmonic Metal Nanoparticle	2.22	84.3	36	[91]
CuS/Polyacrylamide-Carboxymethyl Cellulose (PAAm-CMC) membrane	2021	Plasmonic Metal Nanoparticle	1.613	79	47.2	[10c]

Table 2. continued

Solar Steam Generator (SSG)	Year	Photothermal Materials (PTM)	Water Evaporation Rate Under 1 Sun [kg m^{-2} h^{-1}]	Efficiency [%]	Maximum Surface Temperature [°C]	Ref.
Silver nanoparticle-polyacrylonitrile electrospun nanofiber (Ag@PAN) membrane	2021	Plasmonic Metal Nanoparticle	1.34	76	41.3	[92]
Wood-TA-Fe^{3+}	2020	Plasmonic Metal Nanoparticle	1.85	90	NA	[93]
Copper sulfide ($Cu_{2-x}S$) nanorods/PVA	2020	Plasmonic Metal Nanoparticle	1.27	87	42	[94]
TiN/wood based-carbon foam	2019	Plasmonic Metal Nanoparticle	1.47	92.5	45	[27]
Tungsten trioxide (WO_{3-x})/wood	2019	Plasmonic Metal Nanoparticle	1.28	82.5	42	[95]
Cu_2SnSe_3/Cu2ZnSnSe$_4$-polyurethane foam	2018	Plasmonic Metal Nanoparticle	1.657	86.6	40	[96]
Copper Sulfide (CuS)/polyvinylidene fluoride membrane (PVDFM)	2018	Plasmonic Metal Nanoparticle	1.43	90.4	38.5	[10d]
Cu_9S_5/PVDFM	2018	Plasmonic Metal Nanoparticle	1.173	80.2	36.1	[97]
Ag/diatomite filter paper	2017	Plasmonic Metal Nanoparticle	1.39	92.2	44	[10a]
TiAlON-modified NiO (M-NiO) disc	2017	Plasmonic Metal Nanoparticle	1.13	73	41	[98]
Ti_3C_2 MXene/MMT/Chitosan hydrogel	2022	Semiconductor	1.36	93.7	51	[47]
($Cu_{2-x}Se$)/Nb_2CT_x nanocomposites	2022	Semiconductor	1.2		47.1	[48]
Fe_3O_3 nanoparticle/p(NIPAm-co-PEGDA) hydrogel	2021	Semiconductor	5.12	NA	35	[99]
TiO_2 nanorods (TNRs)/glassy carbon foam	2021	Semiconductor	2.23	67.1	41.4	[11b]
MnO2 nanowires/Chitosan Hydrogels (SPM-CH)	2021	Semiconductor	1.78	90.6	40.8	[100]
Fe_3O_4/polyester (PET) fabric-modified melamine-formaldehyde (mMF)	2021	Semiconductor	1.59	100	47.1	[46b]
Fe3O4/PVA@wood	2021	Semiconductor	1.3	73	58	[11c]
Chitosan/gelatin-based interpenetrating network sponge with melamine-coated titania hollow nanospheres (CG@MPT-h)	2021	Semiconductor	1.13	78.9	34.1	[101]
Ti^{3+}-TiO_2/polyethylene foam	2020	Semiconductor	1.2	77.1	39.8	[102]
Black TiO_2/polystyrene foam	2020	Semiconductor	1.16	77.14	45.4	[11a]
Fe_3O_4/polyvinylidene fluoride-**co**-hexafluoropropylene (Fe_3O_4/PVDF-HFP)	2020	Semiconductor	0.97	53	30	[46c]
$K_2Mn_4O_8$/poly(vinylidene fluoride) PVDFM membrane	2019	Semiconductor	1.18	80.8	38	[103]
Al_2O_3 coated Cu–Si nanowire	2018	Semiconductor	1.37	86	65.1	[104]
Ti_2O_3/cellulose membrane film	2017	Semiconductor	1.32	92	50	[105]

conjugated polymer SSG (ca. 1.3–3.6 kg m^{-2} h^{-1}). However, conjugated polymer SSG contain the lowest efficiency variance (ca. 77–97 %). Semiconductor SSG seem to produce the lowest average water evaporation rate as well as the least efficient, followed by plasmonic metal nanoparticle SSG. Moreover, plasmonic metal nanoparticle produce the lowest result variance for its water evaporation rate, as well as second lowest to conjugated polymer in terms of efficiency showing its performance consistency. With that said, future SSG studies may utilized more carbon-based and conjugated polymer SSG due to its relatively low-cost and high-water evaporation performance. Another alternative may include the incorporation of photothermal combinations such as anodized aluminum oxide haze/GO-rGO/Au,[61] Pt/Au/TiO_2 plasmonic wood carbon,[62] and Ni@C@SiO_2/PVA hydrogel[63] developed by Behera et al., Wang et al., and Yang et al. respectively, to further improve light absorbance, surface temperature increase rate, and surface roughness manipulation to achieve an efficient and high water evaporation rate.

3. Water Absorption/Transport

Besides having an efficient solar absorber, the need of having an optimum water supply is equally as important to generate an efficient water evaporation. As a result, majority of interfacial

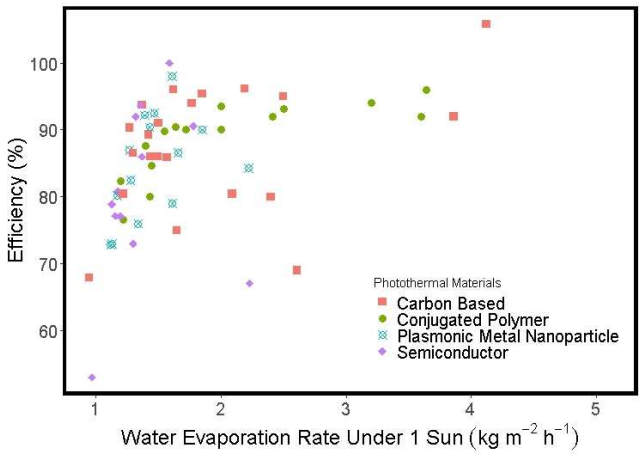

Figure 5. Recent SSG systems with different photothermal materials comparison in relation to water evaporation rate and energy efficiency.

SSG studies have utilized hydrophilic materials into their system improving its ability to absorb/transport water sufficiently for evaporation.[9b,15a,96,106] Water absorption occurs through three different states which are bound water, intermediate water, and free/bulk water (Figure 6a). Bound water contains strong bonding interaction such as hydrogen bonding with functional groups of the network such as carbonyl (–C=O), hydroxyl (–OH), amino (–NH_2), sulfonic (–SO_3H), and carboxylic acid (–COOH).[107] For bulk/free water, it only interacts with other water molecules and has negligible interaction with the network, allowing to diffuse freely. Intermediate water however is bonded with a weaker hydrogen bond and/or dipole-dipole interaction. The presence of intermediate water can usually be determined through Raman spectra in phase and out of phase O–H vibrational mode (ca. 3000–3650 cm^{-1}).[108] An example of this can be seen in the aforementioned VrGO system.[13a] The intermediate water presence generated by the interaction with VrGO oxygenated functional groups (–OH, –C–O–C– or –COOH) and tuned through dynamic compression was evidenced by the two peaks at 3527 and 3624 cm^{-1} of the Raman spectra.[13a] Furthermore, intermediate water is known to undergo thermal transition compared to bulk water. As a result, the intermediate water state has a lower enthalpy for water release than bulk water (Table 3), making it favorable for efficient water transport and evaporation.[109] For example, Zang et al. reported that the reduction of water evaporation enthalpy is corelated by the presence of intermediate water state in their nanofibrous hydrogel/rGO (NHrG) membrane, dominating the interfacial evaporation process (Figure 6a). This was shown through vaporization enthalpy thermogravimetry-differential scanning calorimetry (TGA-DSC) results between bulk water and NHrG membranes, where NHrG vaporization enthalpies are lower despite its high saturation level (Figure 6c). They also found that an increase of GO sheets (absorber) promotes more intermediate water due to its oxygenated functional groups allowing weak hydrogen bonds to form which is consistent

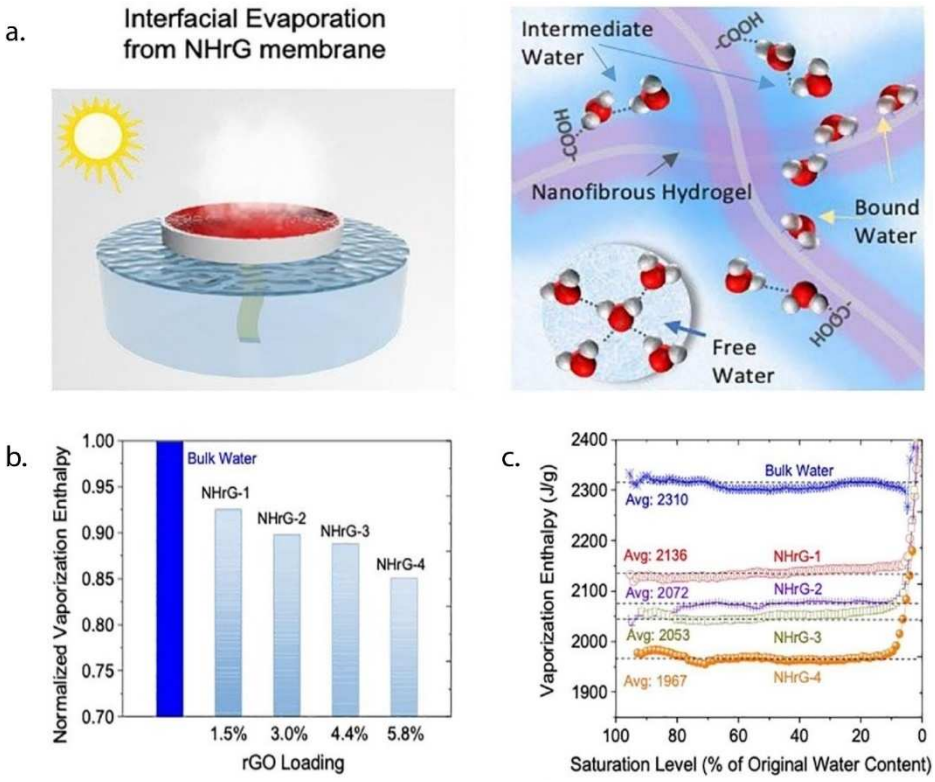

Figure 6. (a) Schematic representation of NHrG interfacial evaporation and water absorption. (b) Comparison of vaporization enthalpies of bulk water and NHrG membrane. (c) Vaporization enthalpies of different NHrG rGO loading. Reproduced with permission.[67] Copyright 2021, Elsevier B.V.

Table 3. Comparison between SSG water evaporation enthalpy and bulk water evaporation enthalpy.

Solar Steam Generator (SSG)	Year	Maximum Surface Temperature [°C]	Water Evaporation Enthalpy [kJ kg^{-1}]	SSG Water Content Evaporation Enthalpy [kJ kg^{-1}]
Three-level pore structure hydrogels (TLPSHs) (rGO/PVA)	2022	45.2	2397	1410
Carbonized cattail (CCT)	2021	30.9	2458	1545
Bryophytes/green moss	2021	35	2442	957
Hydrogel-based ultrathin membrane (HUM) (carbon black/PVA)	2021	37	NA	1130
PVA/SLS-CNT hydrogel (PSCH)	2021	47.1	2375	1525
Nanofibrous hydrogel-rGO membrane (NHrG)	2021	40	2310	2072
PT-1-1 (PMAAc/TMEDA) hydrogel with black carbon-based oily ink	2021	40	≈2500	≈2200
PVA/PPy gel membrane	2021	28	2424	1735
Chitosan/PAAm/PPy hydrogel	2021	40	2462	1384
Agar hydrogel (AHG)/Prussian blue (PB)-cellulose nanofiber (CNF)	2021	36	≈2400	1367
CuS/Polyacrylamide-Carboxymethyl Cellulose (PAAm-CMC) membrane	2021	47.2	2450	1800
Fe_3O_3 nanoparticle/p(NIPAm-co-PEGDA) hydrogel	2021	35	2489.3	1679.5
Interpenetrating polymer networks gel (IPNG) (PVA-activated carbon/PSS)	2020	33	2435	1571
Molybdenum carbide/carbon-based chitosan hydrogel (MoCC-CH)	2020	40.5	NA	2418
Carbonized rice husk biochar (RHB)	2020	88.5	2441.7	1981
PPy/$FeCl_3$ coated melamine foam	2020	65.7	2257	1710
h-LAH hydrogel (PVA-chitosan/PPy)	2019	33.4	2432	1659
Tungsten trioxide (WO_{3-x})/wood	2019	42	2443.86	2401.1
$K_2Mn_4O_8$/poly(vinylidene fluoride) PVDFM membrane	2019	38	2427	2373
Carbonized bamboo	2018	45.5	2477	1519
Capillarity facilitated water transport hydrogel (CTH) (PVA/rGO)	2018	32	≈2400	≈1400
PVA/PPy hierarchically nanostructured gel (HNG)	2018	41.3	2417	1919
PPy coated cotton/polystyrene foam	2018	33.1	2434.1	2411

with Li's results. However, NHrG-2 membrane (2.8 wt% increase of GO loading) produced the highest water evaporation rate of 1.85 kg m^{-2} h^{-1} with 95.4% efficiency (Figure 6b). This shows that bulk water acting as a reservoir to replenish the intermediate water is a contributing factor towards the membrane efficiency. With a constant evaporation of intermediate water, the membrane's efficiency decreased significantly to 85% as produced by NHrG-4 (5.4 wt% increase of GO loading).[67] Besides using DSC, other studies demonstrated their SSGs' low evaporation enthalpy through an alternative dark evaporation test. Under constant temperature and humidity conditions, water evaporation enthalpy can be expressed as Equation (4):

$$H_{water} m_{water} = H_{SVG} m_{SVG} \quad (4)$$

where H_{water} and m_{water} are the bulk water's evaporation enthalpy and mass change, while H_{SVG} and m_{SVG} are the SSG's water evaporation enthalpy and mass change.[9c,64,91]

For example, Zhou et al. used both DSC and dark evaporation method to calculate their interpenetrating polymer network gels (IPNG) evaporation enthalpy in comparison to bulk water. IPNG3 with PSS/PVA ratio of 1.5:1 was shown to have the lowest evaporation enthalpy of 1571 and 860 J g^{-1} by DSC and dark evaporation method respectively compared to other IPNG samples and bulk water (2435 J g^{-1}). As a result, IPNG3 was able to produce the highest evaporation rate of 3.86 kg m^{-2} h^{-1} with 92% efficiency.[9c]

Aside from having low evaporation enthalpy for easy water release, another contributing factor to an efficient water transport is cross-linking density of polymeric networks. Cross-linking density can be measured by several methods such as dynamic mechanical analysis of polymer network's elastic modulus, Flory-Rhener swelling network, nuclear magnetic resonance (NMR) relaxation time, and Flory-Stockmayer Fourier transform infrared spectroscopy (FTIR).[110] Rahaman et al. found that an increase of cross-linker acrylic acid (AAc) in PVA/polyvinyl pyrrolidone (PVP) hydrogel causes a slower water diffusion across the polymer network.[111] Moreover, Wu et al. conducted molecular dynamic study of polyethylene glycol (PEG) hydrogels and observed similar result. Besides a reduce of water diffusion coefficient, an increase of cross-linking density reduces the water content due to reduction of coordination number and water hydrogen bonding.[112] However, an increase of cross-linking density promotes higher mechanical stability of polymer network for durability purposes.[113] For example, Lin et al. reported a dual cross-linked network with chemical cross-link of poly(acrylic acid-*co*-acrylamide-*co*-methylenebisacrylamide) (poly(AAc-*co*-AAm-*co*-MBAA)) and coordination of acrylic-Fe(III). The resultant hydrogel showed a significant increase of elastic modulus, tensile strength, and toughness in comparison to single cross-linked poly(AAc-*co*-AAm-*co*-MBAA) hydrogel.[114]

Furthermore, material surface roughness may affect water transport efficiency. Wang et al. managed to find a correlation between surface roughness, surface energy, and wettability. In short, hydrophilic materials will increase its hydrophilicity when surface roughness is enhanced. This is because an increase of surface roughness allows an increase of surface energy as well as wettability. However, this effect is reversed in terms of hydrophobic material and therefore increases its

hydrophobicity.[115] Despite this, hydrophilic material surface roughness may lead to wetting failure depending on its wetting velocity. Zhao et al. demonstrated that rough hydrophilic surface wettability increases at low wetting velocity. With an increasing wetting velocity approaching its critical value, the surface roughness will inhibit its surface wetting due to the decreased driving force allowing Wenzel to Cassie-Baxter transition to occur.[116]

4. Thermal Insulation

As mentioned previously, solar-thermal energy is the main drive which causes water evaporation in a SSG system. However, the heat generated by the photothermic material may lead to heat loss through conduction, convection, and irradiation which therefore causes an inefficient solar-thermal energy conversion as shown:

$$E_{total} = E_{solar} - E_{radiation} - E_{convection} - E_{conduction} = A\alpha Q_{solar} - A\varepsilon\sigma\left(T_1^4 - T_2^4\right) - Ah(T_1 - T_2) - AQ_{water} \quad (5)$$

where A is the material surface area, α is the light absorption, ε is the emissivity, σ is the Steffan-Boltzmann constant, h is the heat transfer coefficient, T_1 is the surface temperature, T_2 is the ambient temperature, Q_{solar} is the solar irradiance power density, Q_{water} is the heat flux on water surface.[15b,117]

Based on above equation, heat conduction is one of the key contributors to energy lost. With this regard, many systems have employed insulated substrates to reduce the heat loss to bulk water through conduction. For example, Song et al. reported a graphene-based hive (GBH) solar evaporator which consists of polypropylene foam inside of the hive pores as well as hive's outer wall. This leads to heat trapping which avoids heat conduction to the bulk water, reducing the substrate temperature by 10 °C compared to the system without the foam.[118] To construct an optimum insulated substrate, there are factors needed to be considered such as chemical structure, molecular weight, and cross-linking density which are known to be directly proportional to polymer's thermal conductivity.[119] Despite this, a molecular dynamic simulation study of cis-1,4-polyisoprene rubber conducted by Engelmann et al. have shown that the increase of cross-linking density can insignificantly increase thermal conductivity. A noncrosslinked and 9.41 phr (parts per hundred rubber) crosslinked rubber were compared at roughly room temperature. The result shows that a significant increase of thermal conductivity will only appear when the rubber undergoes a mechanical strain caused by coupling of neighboring chains.[120] Moreover, Ni et al. reported a complete opposite effect where a decrease in thermal conductivity is caused by an increase of cross-linking. Polyethylene (PE) with 5% and 10% of crosslinked carbon atoms have a thermal conductivity reduction of 26.6% and 44.2% respectively.[121] Rashidi et al. conducted molecular dynamic (MD) simulation to explain this inconsistency of cross-linking density effect on thermal conductivity. Through MD study of different polymers, they found that thermal conduction travels primarily through nonbonding (van der Waals and electrostatic) interaction as well as covalent bonding. Additionally, cross-linking endorses the shortening of polymer interchain distance, leading to an enhancement of nonbonding interaction between chains which therefore increases thermal conductivity. However, the results showed that thermal conductivity decreases without nonbonding interaction as well as having no change with only covalent interaction and short interchain distance, making nonbonding interaction independent. Furthermore, heat flow analysis of polymer chains using 1 THz acoustic wave propagation showed that heat travels faster through long range nonbonding interaction compared to short range covalent interaction.[122]

Alternatively, an ideal approach is to produce a contactless SSG system which was demonstrated by Cooper et al., eliminating conduction heat loss occurring to bulk water (Figure 7a,b). In this system, water evaporation will occur through heat irradiation instead. However, the contactless design has a low solar-to-vapor conversion efficiency with only 24.6% compared to the common SSG designs.[123] In addition, carbonized cattail-based and cotton/cellulose/carbon-black SSG developed by Zhang et al. and Li et al. respectively seem to have addressed the issue of eliminating convectional heat loss. In both studies, high surface temperature of the illuminated top surface was shown to cause thermal loss through convection and radiation to the lower temperature surrounding environment. Owing to their structural design, these systems both had a temperature gradient between the top and side surfaces. This led to the side surface regaining the energy loss from the environment through evaporative cooling, as the side surface temperature is lower than the surrounding environment. As a result, Zhang et al. and Li et al. attained an apparent efficiency of 105.8 and >100% respectively (Figure 7c).[60]

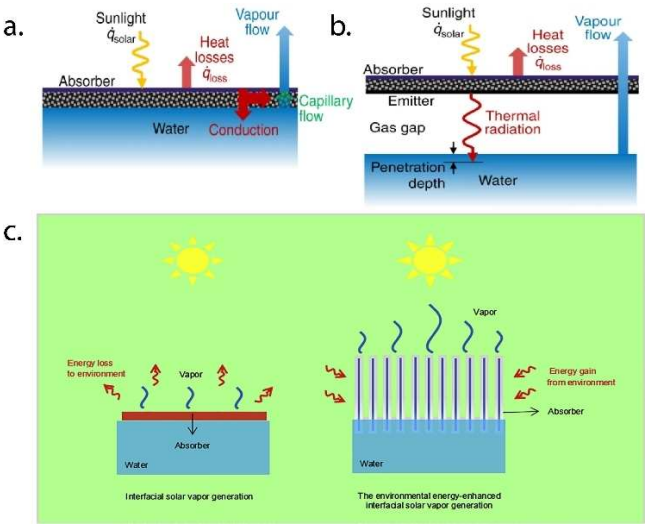

Figure 7. Schematic representations of (a) normal interfacial SSG and (b) contactless SSG systems. Reproduced with permission.[123] Copyright 2018, Nature Communications. (c) Schematic depiction of how SSG systems obtain energy from the environment. Reproduced with permission.[60b] Copyright 2018, Elsevier Inc.

5. Floating Dynamic

Generally, SSG systems are constructed with the intention to float on water surface to avoid any heat loss towards the bulk water for efficient water evaporation. However, the floating dynamic and design of the system are often overlooked. First factor to consider is usually the object's overall density. In general, according to Archimedes' principle an object is likely to float when its overall density is less than the density of water, making its buoyancy force higher than gravitational force.[124] As a result, many studies have used light and porous materials into their SSG system to stay afloat. For example, wood-based SSG coated with candle soot solar absorber produced by Wang et al. was able to achieve an overall low density of 0.106 g cm^{-3} due to its high porosity of 91.7%.[76] Besides this, freeze dried hydrogels are another common porous lightweight material incorporated in many SSG systems.[125] One example of this can be seen in He et al. developed porous acetylene black doped polyacrylamide and sodium alginate dual crosslinked (ACET/PAM/SA-LN(25)) hydrogel SSG which was directionally freeze dried. ACET/PAM/SA-LN(25) hydrogel was able to self-float due to its porous structure obtained from freeze drying compared to regular/nondirectional freeze dried ACET/PAM/SA hydrogel during water swelling (Figure 8a).[126] Yu et al. showed a similar example where the molybdenum carbide/carbon-based chitosan (MoCC-CH) hydrogels prepared by a freeze-drying method can float freely on water surface.[70]

In addition to this, previous studies showed that liquid surface tension contributes to the object's buoyancy force. As a result, elongated hydrophobic objects are able to float in spite of its high overall density.[127] Since wetting can lead to water permeation, hydrophobic materials are ideal solution to be used as a floating platform due to its low surface energy and wettability.[128] When a hydrophobic material is in contact with water, meniscus is formed around the edges of the object and is proportional to the object's cross section perimeter bounded by the triple line. This triple line will adjust along the object's vertical axis according to the amount of gravitational force acted on the object. The buoyancy force is also directly proportional to the triple line contact angle (θ), as well as the object's lateral dimension. With a very small dimension the buoyancy force relies mostly on the liquid's surface tension. The object's volume will influence its buoyancy as the dimension increases. At a certain contact angle, the object's buoyancy force will hit its maximum and will continually decrease with the increasing angle which leads to the object sinking. Liu et al. demonstrated this maximal buoyancy force condition or sinking condition through the parabolic relation given by Equation (6):

$$\widetilde{F_b} = \kappa^2 V(\theta) \tag{6}$$

where $\kappa^{-1} = \sqrt{\gamma/(\rho_L g)}$ is the capillary length, γ is the liquid surface tension, ρ_L is the Laplace pressure difference, g is the gravitational acceleration, and $V(\theta)$ is the extruded liquid total volume.[129]

This can be seen in nature such as the aquatic insect *Dixa langistyla*, which uses its crown-containing hydrophobic hair structure to float and swim near the water's surface. Suzuki et al. showed that by reducing the water surface tension through oil insertion on the insect's crown, the insect lost its ability to swim and float, therefore showing that it does not rely on air bubbles to float but rather its hydrophobic hair.[130] In terms of SSG example, Xu et al. demonstrated their system's floating ability is due to the constructed hydrophobic layer prepared by heated chitosan aggregate on the bottom of a triple layered structure. By using this design, Xu et al. managed to produce 2.41 kg m^{-2} h^{-1} evaporation rate with 92% efficiency.[80] Moreover, Zhang et al. developed a cattail-based SSG which managed to produce up to 4.12 kg m^{-2} h^{-1} water evaporation with 105.8% efficiency, utilized polystyrene foam as a floating material for their cattail solar absorber to float near the water surface (Figure 8b).[60a]

Surface roughness can also potentially influence material floating dynamic besides increasing light and water absorption. Yonemoto et al. found similar results to those reported by Wang et al.[115] between the correlation of surface roughness and wettability. Yonemoto et al. also reported that surface roughness increases material hydrophobicity due to an increase of contact angle and therefore decrease in wettability, while it

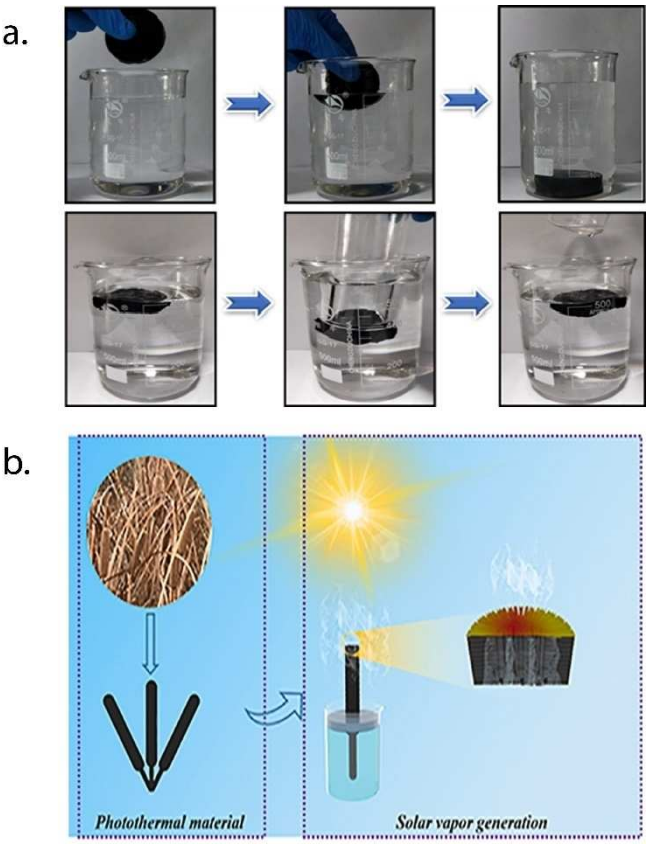

Figure 8. (a) Self-floating comparison of ACET/PAM/SA conventionally made hydrogel (top) with ACET/PAM/SA-LN(25) directional frozen hydrogel (bottom). Reproduced with permission.[126] Copyright 2020, Elsevier Ltd. (b) Schematic depiction of cattail-based SSG undergoing solar steam generation with polystyrene foam utilized to float on water surface, developed by Zhang et al. Reproduced with permission.[60a] Copyright 2021, Elsevier B.V.

is vice versa for hydrophilic material.[131] Parenthetically, surface curvature can affect the material surface energy on a micro/nano scale. Wang et al. studied this correlation through theoretical modelling of Lennard-Jones potential intermolecular interaction between surface particles with surrounding particles. They found that the surface energy increases in a concave surface and decreases in a convex surface relative to a flat surface.[132] Moreover, micro/nano-particles containing surfactants and light oils should also be taken into account to the floating dynamic due to its capability lowering water's surface tension.[133]

6. Water Filtration

6.1. Salt rejection

Seawater metal ions salts are one of the major concerns to be taken into account in freshwater production. At low level concentration, seawater salts may bring health benefits such as reduction of cholesterol and blood pressure, as well as protection from cardiovascular problems and obesity. However, unfiltered seawater containing high level of salts could potentially lead to acute effects such as nausea, vomiting, chronic congestive heart failure, and hypertension.[134] Besides health concerns, salt accumulation on SSG surface can potentially inhibit its solar-to-vapor conversion efficiency due to the lack of light absorption or even heat loss. As a result, many SSG systems have been designed to have salt filtration/rejection capabilities.[135] One example of this design can be seen through natural and active salt diffusion. Salt diffusion back to the bulk water is caused by a gradient salt concentration between the evaporator surface and the water source.[136] A 2D/3D transforming rGO/cellulose sponge-based SSG reported by Wang et al. is an example of SSG which uses natural diffusion to dispose salt. After 8 h of evaporation, this sponge-based SSG showed low content of salt fouling/accumulation throughout the process. However, salts were then automatically dissolved back after 2 h of no light exposure. However, salt accumulation still occurs during SSG evaporation which inhibits the water evaporation performance shown by the slight decrease (4.12 to 4.08 $kg\,m^{-2}\,h^{-1}$) throughout continuous 8 h evaporation due to salt fouling.[137] On the other hand, active salt diffusion can prevent salt accumulation due to its fast water replenishing of evaporated brine on the surface.[136] For example, PPy coated VMP foam reported by He et al. with 1.410 $kg\,m^{-2}\,h^{-1}$ evaporation rate and 88.3% efficiency demonstrated excellent salt-rejection. The demonstration involved placing NaCl on top of the foam throughout the SSG testing under 1 sun. They found that the accumulated salt was able to dissolve back to the water source after 1.13 h of evaporation, leaving no salt to accumulate on the surface due to the interconnected macropores of the VMP which allows fast water transport to replenish vaporized brine on the surface. Moreover, the freshwater generated contained significantly low concentration of salt ions compared to WHO standards.[138]

Besides salt diffusion, some studies have suggested another type of salt rejection design such as "Donnan repulsion" method. This method relies on electrostatic repulsion of ions through the application of ion barrier on the SSG membrane.[139] For example, PPy coated monolithic porous ionic polymers (PIPs) developed by Wang et al. demonstrated excellent salt rejection capability. This is due to the imidazole cationic ion barrier which prevents any cations in the saline solution to permeate through the membrane. As a result, a significant reduction of salt ions (K^+, Ca^{2+}, Na^+, Mg^{2+}) obtained from Dalian seawater was shown. In addition, all PIPs showed consistent water evaporation performance under seawater for 6 h, as well as insignificant change of water evaporation rate in 30 wt% NaCl saline water compared in pure water. Furthermore, no salt crystals accumulation occurred in the polymer as shown by XRD spectrum.[83] Similarly, Kospa et al. managed to generate similar findings of salt rejection capabilities of their CuO-rGO/PANI membrane by "Donnan repulsion". Their utilization of emeraldine salt (ES) formation of polyaniline (PANI) as their PIP allowed this membrane to have "Donnan repulsion" due to the cationic quinonoid and benzenoid structure of the ES-PANI, causing charge-charge repulsion with the cations in the saline water. As a result, 99% salt ions (Ca^{2+}, Na^+, K^+, Mg^{2+}) rejection was achieved by solar steam generation using natural seawater demonstrated by inductively coupled plasma-optical emission spectrometry (ICP-OES). Furthermore, CuO-rGO/PANI membrane was able to consistently produce 2.02 $kg\,m^{-2}\,h^{-1}$ water evaporation with 10 wt% artificial saline water under 1 sun for 10 cycles. Additionally, no salt accumulation was found after 20 days evaporation under real sun.[140]

Another salt rejection design strategy is to modify the surface topography of the SSG such as having hydrophilic/hydrophobic Janus membrane. interface layer, allowing only water vapors to diffuse through and filtering salts behind. Xu et al. managed to integrate this design in their water lily-like SSG system containing hydrophobic etched Cu foam coated with Al_2O_3 and CB layer, with an additional polystyrene foam bottom layer. In between these two layers, a water vesicle was formed to store the absorbed water via the bottom layer holes, which act as a vesicle bundle for water transport. This system managed to generate water evaporation rate of 1.31 $kg\,m^{-2}\,h^{-1}$ DI water, 1.28 $kg\,m^{-2}\,h^{-1}$ 10 wt% brine water, and 1.27 $kg\,m^{-2}\,h^{-1}$ 30 wt% wastewater under 1 sun illumination with 27–28 °C temperature range, ~30% humidity, and a respective efficiency of 79.8%, 78.5%, and 77.2%.[141] Similarly, Wu et al. constructed a spherical SSG system with a hydrophobic solar absorber interface layer. This system contains polystyrene foam layered with cellulose as the substrate, PDA hydrophilic layer, PPy hydrophobic solar absorber layer, and PDA protection coating as the end layer. Owing to the continuous water evaporation, small quantity of salt was able to accumulate at the top interface layer. However, its hydrophobic lightweight spherical core allows the system to rotate in all directions due to the mass imbalance triggered by the small amount of salt accumulation, bringing the salt down to the bulk water and diffusing it. This system was able to produce evaporation rate of respectively 2.6, 2.32, and 2.06 $kg\,m^{-2}\,h^{-1}$ of

3.5, 7, and 20 wt% NaCl solution under 1 sun for 8 h desalination.[142] Furthermore, Xiong et al. produced and tuned the hydrophilicity/hydrophobicity of their rGO/hydroxyapatite nanowires (HN) paper through the heat treatment duration. Qualitatively, the hydrophobic paper was able to avoid salt accumulation on its interface after 1 sun illumination desalination of 3.5 wt% NaCl solution, in comparison to the hydrophilic counterpart. However, this comes with a cost of the reduction of water evaporation rate. The hydrophobic paper was able to evaporate 1.25 kg m^{-2} h^{-1} pure water, while the hydrophilic paper evaporated 1.48 kg m^{-2} h^{-1}.[143] Besides using hydrophobic interface, thermocapillary effect is another option that can be used without sacrificing water evaporation performance. Furthermore, salt diffusion back to water source may lead to brine production which therefore could have potential environmental impact. Brine discharges to the marine environment have shown to affect marine species such as fish and benthic organisms. This is because brine's high salinity level induces irreversible cell dehydration which could lead to a long-term extinction.[144]

Thermocapillary effect aka. Marangoni effect is the change of liquid surface tension caused by temperature gradient. In this effect, liquid has the tendency to flow from high to low temperature due to low higher surface tension at low temperature.[145] By using this method, salt accumulation can be deposited at a specific site to be harvested or disposed.[136] For example, Huang et al.[146] and Wu et al.[147] designed their SSG system to contain a cone structure array on the interface. With this structure, thermocapillary effect can take place allowing the salt water to travel from the bottom to the top interface, accumulating the salt at the tip of the cone for easy removal, owing to the temperature gradient, as mentioned previously regarding surface morphology (Figure 9a). As a result, salt accumulation was spatially localized hence water evaporation performance will not be significantly reduced. Huang et al. constructed PDA/PVA system managed to produce a high evaporation rate of 2.94 kg m^{-2} h^{-1} 25 wt% NaCl solution with a slight (7.1%) decrease of evaporation rate under continuous (150 min) evaporation and 94.5% efficiency under 1 sun. Moreover, the PDA/PVA system was able to majorly filtrate salt ions (Na^+, K^+, Mg^{2+}, Ca^{2+}) contained in the seawater, as well significantly reduce the Na^+ concentration despite evaporating high saline water concentration (3.5, 7.5, 15, 25 wt%). Additionally, PDA/PVA system was able to completely filter organic dyes (methylene blue (MB), rhodamine B (RhB), methylene orange (MO)) demonstrated by the comparison of contaminated and filtered water UV absorption.[146] Similarly, Wu et al. constructed CNTs/polyacrylate resin system achieved consistent 2.63 kg m^{-2} h^{-1} 25 wt% NaCl solution continuous evaporation and a net evaporation of 1.46 kg m^{-2} h^{-1} with $>$96% efficiency under 1 sun. This resin system also managed to significantly reduce salt (Na^+, Mg^{2+}, K^+, Cu^{2+}) and heavy metal ions (Co^{2+}, Cu^{2+}, Na^+).[147] To completely avoid salt accumulation at the surface, saline water can also be directed away from the SSG surface. For example, Li et al. demonstrated salt migration SSG system using superhydrophilic carbonized green algae (SHCGA) as their solar absorber membrane. In this system, Li et al. utilized cotton threads to redirect the salt crystallization to avoid salt accumulation at the surface, where one end of the thread touches the saline solution and the other is redirected away from the system. This system relies on the coffee ring effect which allows the saline solution to capillary flow outward from the center. Since the saline solution has high adhesion towards the cotton thread, the saline solution will travel through the thread leaving continuous salt to crystalize throughout the entire evaporation process. To avoid the expanding salt crystallization from polluting the captured freshwater, Li et al. developed a container to capture excess salt from the expanding crystallization. With this design, Li et al. reported no salt accumulation on the membrane surface after 15 days of continuous evaporation of artificial saline water (20 wt% NaCl solution).[148]

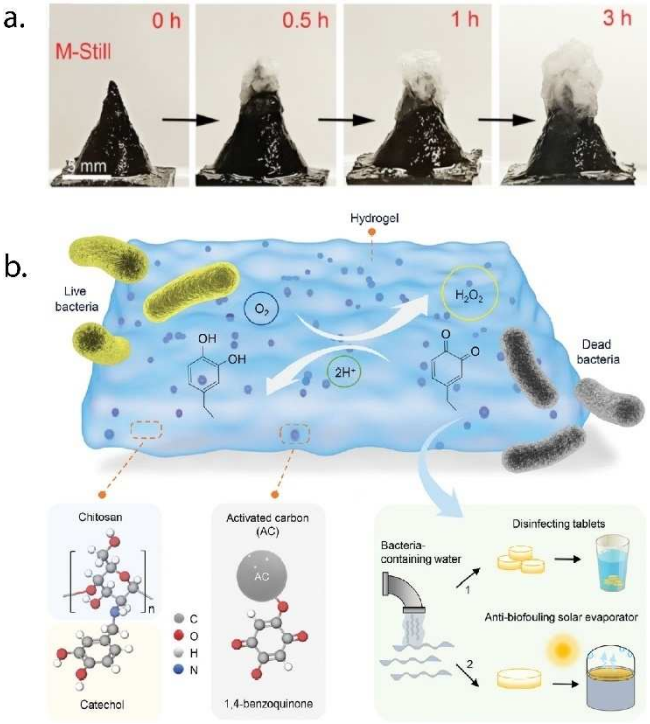

Figure 9. (a) Salt-dumping by PDA/PVA SSG system. (b) Schematic representation of ABH anti-biofouling by using reactive oxygen species developed by Huang et al. and Guo et al., respectively. Reproduced with permission.[146,159] Copyright 2021, Wiley-VCH GmbH.

6.2. Microorganisms and micropollutants

Besides salt filtration, contaminants such as micropollutants, bacteria, and algae must be highly considered in freshwater production due to health implications. For example, micropollutants are known to induce neurotoxicity, cancer, and leukemia, while bacteria and algae can lead to infectious disease and odor compounds production respectively.[149] Contaminants can be removed through our current water treatment process which involves coagulation, flocculation,

sedimentation, sand filtration, disinfection (chlorination, UV treatment, and O_3/H_2O_2 reactive species), and nutrient removal.[150] This current process however is inefficient, leaving some contaminants unremoved as demonstrated by water treatment efficiency study from Nam et al. They investigated and measured 14 micropollutants in a water treatment plant in Seoul, Korea. Based on these results, 12 out of 14 selected micropollutants were detected in the influent source and 11 were detected in the final effluent source at the part per trillion level with an overall removal efficiency ranging from 6–100%. Additionally, Nam et al. stated that highest micropollutants removals occur at the coagulation stage due to the incorporation of adsorption to clay particles and UV photodegradation. This stage however contains a wide range of efficiency between 9% - 100%. Nam et al. also implied that the removal efficiency depends on the micropollutants' physicochemical properties and photo-sensitivities.[151] VBNC bacteria is another major health concern due to being undetectable using cultured-dependent method. Moreover, Guo et al. and Zhu et al. showed that VBNC bacteria are not able to be treated/removed. Guo et al. managed to detect 0–10^2 cells/100 mL in the treated chlorinated water using PMA-qPCR, where Zhu et al. detected ~10^2–10^7 cells mL^{-1} in 2–12 mg mL^{-1} chlorinated water.[152] In addition, Zhu et al. reported that VBNC are also UV resistant despite having nucleus damage where ~10^3–10^7 cells mL^{-1} were still detected when exposed to 0–1000 mJ cm^{-2}. Zhu et al. also mentioned that VBNC bacteria are still able to maintain its pathogenic nature and potentially be pathogenic again from resuscitation.[153]

With regards to contaminant removal, water treatment ideas have been applied in previous SSG studies. The most common water treatment method used in SSG systems is photocatalytic degradation. This involves recombination of electron-hole pairs which can interact with surrounding electron donors or hydroxide ions to produce reactive species that can degrade any contaminants.[154] This can be seen in previous examples SSG systems such as from Huang et al.[146] and Wu et al.[147] CuO-rGO/PANI membrane designed by Kospa et al. was also able to filter out organic dyes (MO, MB, RhB) and oil contaminated water besides salt ions. The oil rejection property can be attributed to the ES-PANI hydrophilic and oleophobic characteristics which allows the system to absorb/transport water while removing oil-water emulsion.[140] Other studies such as Zhao et al., claimed that their constructed Cu@CuO/CG aero Janus membrane was able to filter micropollutants such as organic dyes (rhodamine B, methylene blue, and methyl orange) as well as heavy metal ions (Cd^{2+}, Pb^{2+}, and Cr^{2+}) when exposed under 1 sun. According to the high-performance liquid chromatographic (HPLC) results, the aero Janus membrane was able to remove over 99% of the organic dyes ($>10^2$ from initial ppm concentration) and heavy metal ions ($>10^4$ from initial ppm concentration). Besides micropollutants, this Janus membrane was able to decontaminate bacterial (*E. coli*), viral (EV71), and parasitic contaminants (Schistosoma eggs) under 1 sun exposure as shown by a significant reduction count.[155] Unlike other micropollutants, volatile organic compounds (VOCs) are able to penetrate SSG membrane. Song et al. managed to produce a mesoporous and tortuous oxygen-rich m-TiO_{2-x} nanofibrous membrane (NFM) which can generate free radicals under sunlight for photocatalytic degradation of VOCs.[156] Furthermore, the tortuous structure of this membrane helps to increase VOCs removal efficiency due to a longer retention time of VOCs passing through the membrane. As a result, the concentration of phenol VOCs used for simulation decreases significantly to 0.45 mg L^{-1} from an initial 10 mg L^{-1} under 1 sun. Moreover, this membrane was able to reduce phenol concentration up to <0.8 mg L^{-1} in a 30-day cycle under 1 sun for 4 h per 2 days.[157] Another approach for bacterial removal can be seen through Guo et al. constructed anti-bacterial hydrogels (ABH) containing mixture of catechol-functionalized chitosan (CCS) and quinone-anchored activated carbon (QAS). The combination of these materials allows ABH to have antibacterial and anti-biofouling properties. Bacterial cells are eliminated through the production of reactive oxygen species (ROS) such as $^{\bullet}O_2^-$ and H_2O_2 caused by O_2 reaction of catechol group (Figure 9b). ROS are known to oxidize iron-sulfur (4Fe–4S) clusters by the Fenton reaction which leads to DNA and enzyme breakdown, causing metabolic defects.[158] Therefore, ABH exhibited a removal efficiency of $>97\%$ (5 log inactivation) eliminating *B. subitilis* and *E. coli*, and 99.9% (6 log inactivation) removal efficiency of *P. aeruginosa* in 60 min under ambient pressure and room temperature. In comparison, water evaporation without ABH only achieved $<85\%$ (<1 log inactivation) removal efficiency for all three types of bacteria. In addition, ABH can be regenerated by immersing in sodium bisulfite solution for 2 h, reducing quinone group back to catechol.[159] In addition, Ebrahimi et al. demonstrated their antibacterial system poplar wood coated rGO/Ag NPs by having rGO and Ag NPs as the main contributing factors which inhibit the growth of bacteria. Ebrahimi et al. stated that rGO are known to induce bacterial cell membrane damage due to its sharp edges.[160] This antibacterial activity is also in conjunction with Ag NPs, releasing Ag^+ ions which interact with enzyme in bacterial cell metabolism that leads to metabolic failure. In this study, *Staphylococcus aureus* was used to test the bacterial resistance through monitoring the growth inhibition rate (GI%) by its optical density at 630 nm (OD_{630}) measurement. The result showed a significant (1.4) GI% of wood coated rGO/Ag NPs compared to bare wood which did not inhibit any bacterial growth in 24 h.[161]

7. Challenges and Perspective

As discussed, the development of an efficient SSG system is affected by many factors such as the usage of photothermal material (PTM) with high solar-to-vapor conversion efficiency as an evaporator, a hydrophilic water absorber containing low evaporation enthalpy for sufficient water transport, a high thermal insulating substrate to reduce thermal loss produced during evaporation to the surrounding environment, filtration/antifouling property, and floatation ability to undertake interfacial SSG. These factors represent a knowledge gap. Firstly, cost to performance ratio in producing SSG is still a determining

factor in constructing a feasible SSG system. The few recent SSG feasibility studies are compared in Figure 10.

The carbon black/PVA hydrogel-based SSG (HUM) developed by Lu et al. currently seem to provide the best cost to performance of 2.4 kg m^{-2} h^{-1} at only \$0.36 m^{-2} compared to other SSG systems. The water production cost of HUM-based hydrogel was calculated to be ~\$0.3–1.03 m^{-3}. This therefore provides a potentially feasible water generation system as its water production cost is less than our current reverse osmosis (RO) desalination system which is ~\$0.5–1.9 m^{-3}. However, the downside of this HUM-based SSG is that it produces a relatively low solar-to-vapor conversion efficiency of 80% compared to most SSG systems.[9a] In contrast, Xu et al. constructed CNTs/starch hybrid biohydrogel SSG managed to produce the highest water evaporation rate of 2.77 kg m^{-2} h^{-1} with a relative high efficiency of 88% and cost of \$14.65 m^{-2}. Despite this, they claimed that this hybrid biohydrogel system would have a water production cost of 189 g h^{-1} $\$^{-1}$. A simple conversion to \$ L^{-1} is done to facilitate a water production comparison cost between different studies. Therefore, this hybrid biohydrogel would have water production cost of ~\$5.3 L^{-1}.[162] In comparison to the HUM hydrogel, this system would produce ~ \$0.0003–0.001 L^{-1} which is significantly cheaper than the hybrid biohydrogel. Therefore, this hybrid biohydrogel would not be a feasible water generation system to potentially replace current desalination system such as RO. Moreover, a recent SSG example containing rGO/Ag/Wood developed by Ebrahimi et al.

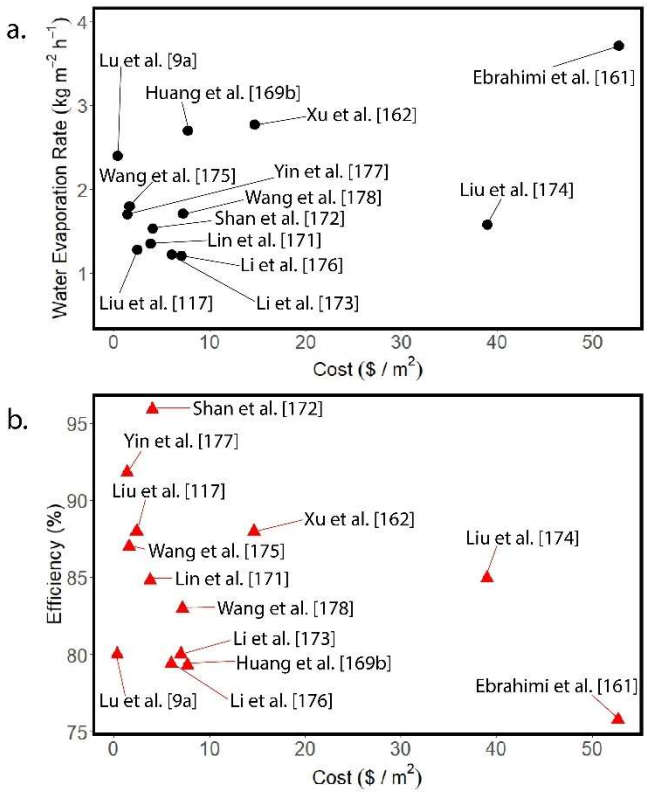

Figure 10. Plot of cost to (a) water evaporation rate and (b) efficiency of recent SSG systems.

managed to produce a promising water evaporation rate of 3.71 kg m^{-2} h^{-1}. Despite this high performance, the cost of this system is very expensive which was shown to be \$52.706 m^{-2}. As a result, the water production cost of this system was demonstrated to be \$0.011 cm^{-3} h^{-1}. When converted to \$ L^{-1}, this can be approximated to be \$11 L^{-1}, doubling the price of the previous hybrid hydrogel example.[161]

Another challenge is the lack of understanding in bacterial filtration mechanism. As mentioned previously, VBNC is a state where a population of culturable cells lose their ability to replicate however remain viable.[163] Additionally, VBNC bacteria may not be treatable by our current water treatment process and therefore making them a major health threat.[152,153] Most bacteria are known to enter VBNC state to survive disinfection treatments such as chlorination and UV exposure.[164] Despite this, Ye et al. reported that it is still possible to reduce the number of VBNC bacteria through longer UV/chlorine treatment with residual chlorine maintained.[165] The results found from this study demonstrated that long UV/chlorine treatment is only effective to certain bacteria types such as *P. aeruginosa*, *S. aureus*, and *Shigella* spp. where their VBNC cells are below 0 CFU. Other type such as *E. coli* VBNC was not effectively removed after treatment. Moreover, UV/chlorine effectiveness depends on the number of bacteria present. As shown in the result, the number of bacteria in the winter water samples was significantly larger compared to spring, autumn, and summer samples. The significant bacteria amount therefore leads to accelerated chlorine decay. As a result, VBNC types of bacteria, such as *P. aeruginosa*, *S. aureus*, and *Shigella* spp. which were effectively removed, could not be treated, and therefore remained despite longer UV/chlorine treatment. Alternatively, studies such as Shao et al. have reported a potential solution in reducing the amount of VBNC bacteria. Atmospheric-pressure air liquid discharge plasma (ALDP) method was investigated in treating VBNC in comparison to conventional chlorine disinfection method. The result demonstrated that ALDP was able to significantly reduce (10^2–10^3 cells mL^{-1} times more) the amount of *E. coli*, *P. aeruginosa*, *Salmonella* sp., and *S. aureus* VBNC compared to chlorination treatment due to its reactive oxygen species (ROS).[164c]

Currently, the SSG performance benchmark is determined through its water evaporation rate and solar-to-vapor conversion efficiency. However, water evaporation rate may not be the most suitable method in evaluating a SSG performance. One of the reasons for this is water evaporation results produced by previous SSG are not normalized and may vary depending on experimental settings. This can be seen from the different evaporation rate results of water itself (control) obtained in different studies. For example, Hao et al.[88] and Sun et al.[166] reported their pure water evaporation rate to be relatively similar which are 0.19 and 0.25 kg m^{-2} h^{-1} respectively. However, another study conducted by Sun et al.[167] and Li et al.[168] seem to produce 0.389 and 0.44 kg m^{-2} h^{-1}, which roughly doubles the amount reported for the prior studies. Owing to the inconsistency of evaporation results between studies, it may be suitable to benchmark the water production difference/enhancement factor (PEF) of a SSG instead. For example, the

study conducted by Hao et al. managed to produce a PPy-coated cotton fabric with polystyrene foam (PPy/cotton-foam) system with 1.2 $kg\,m^{-2}\,h^{-1}$ water evaporation rate. Compared to the previously mentioned studies (Table 5), this system has the lowest evaporation rate out of all four studies. Nevertheless, this PPy/cotton-foam system had the highest PEF and achieved 6.32 times higher water evaporation rate than pure water evaporation.

In contrast, the SP film composed of carbon soot and PVA developed by Sun et al. had a higher water evaporation rate of 1.5 $kg\,m^{-2}\,h^{-1}$. However, due to the higher pure water evaporation (0.389 $kg\,m^{-2}\,h^{-1}$) the SP film showed a lower PEF of 3.86, indicating limited enhancement of water evaporation (Table 5). Therefore, the SSG performance should be benchmarked based on its enhancement factor rather than the water evaporation rate, for a fair comparison and to reveal the potential for practical application in future studies. Currently, the majority of SSG systems were tested under steady and similar circumstances (water evaporation under 1 sun, no wind etc.).[63,98,169] There are also some studies showing that the introduction of external factors can significantly enhance their internal evaporation results. For example, Li et al. claimed their 3D porous carbon foam SSG was able to achieve evaporation rates of 10.9 or 2.5 $kg\,m^{-2}\,h^{-1}$ with or without a convectional air flow of 6 $m\,s^{-1}$.[170]

In summary, our current increasing water demand has pushed us to find alternative solutions to obtain cleaner and cheaper freshwater production. Based on previous studies, SSG has demonstrated its potential as a great alternative to our current and ongoing desalination systems, owing to its cost-effectiveness and environmentally friendly freshwater generation. To create an efficient SSG system, there are factors that are needed to be considered such as:

1. Selecting an appropriate solar absorber to obtain efficient solar-thermal energy conversion to induce water evaporation. The most widely used solar absorbers are plasmonic metals, inorganic semiconductors, conjugated polymer, and carbon-based material. This is attributed to their broad and selective (UV to IR) absorption range to harvest and convert majority of the solar energy to heat.
2. Incorporating a hydrophilic, low vaporization enthalpy, and thermally insulated absorbent/substrate for efficient water transport and evaporation. Hydrophilic absorbents can attract and interact with water molecules due to its oxygenated functional groups. Furthermore, adjusting the material hydrophilicity may introduce more intermediate water interactions. This then leads to a lower water vaporization enthalpy for a more efficient water transport and evaporation. Additionally, thermally insulated substrate can prevent energy loss through conduction, convection, and/or radiation to bulk water as well as surrounding environment during evaporation, allowing to increase SSG's overall solar-to-vapor conversion efficiency.
3. Tuning SSG material macro/micro-structure such as surface topography and overall porosity. As discussed, surface roughness has been attributed to increasing material optical absorption and wettability. This therefore influence the solar-to-vapor conversion efficiency, water transport, and floating dynamic. Moreover, strategic topographical design such as Janus membrane and cone structure array has been emphasized to help in dealing with salt and micropollutant filtration. Besides increasing light and water absorption,

Table 4. Comparison of cost with performance for recent SSG systems (2017–2022).

Material	Water Evaporation Rate [$kg\,m^{-2}\,h^{-1}$]	Efficiency [%]	Cost [$\$\,m^{-2}$]	Year	Ref.
Reduced graphene oxide, silver, and wood	3.71	75.75	52.706	2022	[161]
Carbon black and PVA	2.4	80	0.36	2021	[9a]
Carbon nanotubes (CNTs) and starch	2.77	88	14.65	2021	[162]
Ceramic fiber-based activated carbon-carbon black composite	1.7	91.8	1.38	2021	[177]
Carbonized towel-gourd sponge paper	1.53	95.9	4	2020	[172]
Tannic acid, APTES, Fe2(SO4)3, and PU sponge	1.8	87	1.6	2020	[175]
Gold nanoparticle and PVA	2.7	79.3	7.7	2020	[169b]
Graphene cotton paper-based	1.711	83	7.16 ($3.22/0.45 m^2)	2020	[178]
Carbonized kelp, fiber cotton, and polystyrene foam	1.351	84.8	3.8	2019	[171]
Carbonized biochar, EPE foam, and nonwoven fabric	1.21	80	7	2018	[173]
Biomass mesoporous carbon, geopolymer (AlO6 and SiO4), and polystyrene foam	1.58	84.95	39	2018	[174]
Activated carbon fiber felt	1.22	79.4	6	2018	[176]
Carbon black, fiber-rich paper, and EPS foam	1.28	88	2.38	2017	[117]

Table 5. Comparison of enhancement factors for various SSG systems.

Solar Steam Generator (SSG)	Pure Water Evaporation Rate [$kg\,m^{-2}\,h^{-1}$]	SSG Water Evaporation Rate [$kg\,m^{-2}\,h^{-1}$]	Enhancement Factor (PEF)	Year	Ref.
PPy/cotton-foam	0.19	1.2	6.32	2018	[88]
Carbonized Sunflower Heads	0.25	1.51	6.04	2019	[166]
SP film (carbon soot/PVA)	0.389	1.5	3.86	2021	[167]
Carbon-coated fabrics with tunable water delivery property (CTWD)	0.44	1.33	3.02	2019	[168]

porosity also contributes to the likeliness for a material to float.

Future SSG studies may need to address a feasibility study on a scale-up prototype SSG, which includes cost to performance optimization and long-term stability test. Furthermore, the lack of knowledge behind VBNC bacteria in water treatment still puts a challenge in the topic of SSG water filtration. Besides just investigating the detection of culturable bacteria, future SSG studies may need to further investigate the material filtration effectiveness through quantifying VBNC bacteria detected in the filtered water by using methods, such as PMA-qPCR.

8. Conclusion

In this comprehensive review, we have highlighted recent achievements in the development of SSG materials for water production. Photothermal materials with high solar-to-vapor conversion efficiencies and low cost, as well as research in hydrophilic matrices that can facilitate water absorption/transport and lower evaporation enthalpies, will continue to advance. Although other strategies, such as thermal insulation, floating dynamic, and salt/bacterial filtration, were also proposed to further improve water production performance, a significant gap between laboratory designs and practical application remains. Research bottlenecks that hinder the development of SSGs include the lack of testing and performance evaluation standardization. The cost-performance ratio and the enhancement factor were proposed to fully evaluate the commercial potential of SSG systems. A promising approach to boost current SSG performance lies in the combination of solar absorber and hydrophilic absorbent selection, as well as finely controlling material microstructures to achieve a balance of water transport and evaporation, along with floatability. Future advances in this field will mainly focus on developing more effective cost-to-performance generating materials, as well as producing new generation SSG filtration systems that would include VBNC disinfection.

Acknowledgements

Q. F. acknowledges the Australian Research Council under the Future Fellowship (FT180100312). C. O. acknowledges support of the Australian Government Research Training Program Scholarship from the University of Technology Sydney. Open Access publishing facilitated by University of Technology Sydney, as part of the Wiley - University of Technology Sydney agreement via the Council of Australian University Librarians.

Conflict of Interest

The authors declare no conflict of interest.

Keywords: evaporation · photothermal materials · solar steam · solar-to-vapor conversion · water purification

[1] a) W. W. A. P. UNESCO, UNESCO, **2020**; b) C. J. Vörösmarty, P. Green, J. Salisbury, R. B. Lammers, *Science* **2000**, *289*, 284–288.
[2] a) A. F. S. Foureaux, V. R. Moreira, Y. A. R. Lebron, L. V. d. S. Santos, M. C. S. Amaral, *Sep. Purif. Technol.* **2021**, *256*, 117797; b) Y. Wada, M. Flörke, N. Hanasaki, S. Eisner, G. Fischer, S. Tramberend, Y. Satoh, M. T. H. van Vliet, P. Yillia, C. Ringler, P. Burek, D. Wiberg, *Geosci. Model Dev.* **2016**, *9*, 175–222; c) M. Tesfaye, S. Moges, A. M. Melesse, Z. Agide, *IJEWR* **2021**; d) A. P. P. Carvalho, R. Lorandi, E. G. Collares, J. A. Di Lollo, L. E. Moschini, *Agric. Ecosyst. Environ.* **2021**, *319*, 107508; e) M. Le Page, Y. Fakir, L. Jarlan, A. Boone, B. Berjamy, S. Khabba, M. Zribi, *Hydrol. Earth Syst. Sci.* **2021**, *25*, 637–651.
[3] a) H. H. G. Savenije, *Phys. Chem. Earth Part B* **2000**, *25*, 199–204; b) A. Boretti, L. Rosa, *npj Clean Water* **2019**, *2*, 15; c) G. Mao, H. Hu, X. Liu, J. Crittenden, N. Huang, *Environ. Pollut.* **2021**, *275*, 115785.
[4] a) O. L. Miller, A. L. Putman, J. Alder, M. Miller, D. K. Jones, D. R. Wise, *J. Hydrol. X* **2021**, *11*, 100074; b) Z. Zhang, E. Getahun, M. Mu, S. Chandrasekaran, *JAWRA*; c) T. M. N. Carvalho, F. de Assis de Souza Filho, *Water Resour. Manage.* **2021**.
[5] a) S. Rizvi, R. Rustum, M. Deepak, G. B. Wright, S. Arthur, *Water Supply* **2020**, *21*, 1144–1156; b) D. U. Lüdtke, R. Luetkemeier, M. Schneemann, S. Liehr, *Water* **2021**, *13*, 260; c) D. Kim, T. Yim, J. Y. Lee, *Energy* **2021**, *231*, 120915; d) H. Abu-Bakar, L. Williams, S. H. Hallett, *npj Clean Water* **2021**, *4*, 13.
[6] a) A. H. M. Saadat, M. S. Islam, P. Fahmida, A. Sultana, *J. Sci. Res.* **2018**, *10*, 77–97; b) V. G. Gude, N. Nirmalakhandan, S. Deng, *Renewable Sustainable Energy Rev.* **2010**, *14*, 2641–2654; c) J. Leijon, C. Boström, *Desalination* **2018**, *435*, 161–171; d) G. Micale, A. Cipollina, L. Rizzuti, in *Seawater Desalination: Conventional and Renewable Energy Processes* (Eds.: G. Micale, L. Rizzuti, A. Cipollina), Springer Berlin Heidelberg, Berlin, Heidelberg, **2009**, pp. 1–15.
[7] a) J. Morillo, J. Usero, D. Rosado, H. El Bakouri, A. Riaza, F.-J. Bernaola, *Desalination* **2014**, *336*, 32–49; b) V. G. Gude, *Water Res.* **2016**, *89*, 87–106; c) Y. Tu, R. Wang, Y. Zhang, J. Wang, *Joule* **2018**, *2*, 1452–1475; d) N. Ghaffour, T. M. Missimer, G. L. Amy, *Desalination* **2013**, *309*, 197–207; e) E. Jones, M. Qadir, M. T. H. van Vliet, V. Smakhtin, S.-M. Kang, *Sci. Total Environ.* **2019**, *657*, 1343–1356.
[8] a) *Energy News* **2021**, *39*, 11–12; b) S. J. Davis, N. S. Lewis, M. Shaner, S. Aggarwal, D. Arent, I. L. Azevedo, S. M. Benson, T. Bradley, J. Brouwer, Y.-M. Chiang, C. T. M. Clack, A. Cohen, S. Doig, J. Edmonds, P. Fennell, C. B. Field, B. Hannegan, B.-M. Hodge, M. I. Hoffert, E. Ingersoll, P. Jaramillo, K. S. Lackner, K. J. Mach, M. Mastrandrea, J. Ogden, P. F. Peterson, D. L. Sanchez, D. Sperling, J. Stagner, J. E. Trancik, C.-J. Yang, K. Caldeira, *Science* **2018**, *360*, eaas9793; c) C. Butler, A. Denis-Ryan, P. Graham, R. Kelly, L. Reedman, I. Stewart, . Yankos, *Decarbonisation Futures: Solutions, Actions and Benchmarks for a Net Zero Emissions Australia*, ClimateWorks Australia, **2020**.
[9] a) H. Lu, W. Shi, F. Zhao, W. Zhang, P. Zhang, C. Zhao, G. Yu, *Adv. Funct. Mater.* **2021**, *31*, 2101036; b) F. Zhao, X. Zhou, Y. Shi, X. Qian, M. Alexander, X. Zhao, S. Mendez, R. Yang, L. Qu, G. Yu, *Nat. Nanotechnol.* **2018**, *13*, 489–495; c) X. Zhou, Y. Guo, F. Zhao, W. Shi, G. Yu, *Adv. Mater.* **2020**, *32*, 2007012.
[10] a) J. Fang, Q. Liu, W. Zhang, J. Gu, Y. Su, H. Su, C. Guo, D. Zhang, *J. Mater. Chem. A* **2017**, *5*, 17817–17821; b) H.-W. Zhu, J. Ge, H.-Y. Zhao, L.-A. Shi, J. Huang, L. Xu, S.-H. Yu, *Sci. China Mater.* **2020**, *63*, 1957–1965; c) J. Chen, D. Wang, X. Li, H. Sun, H. Zhao, Y. Li, X. Liu, G. Shi, *ACS Appl. Polym. Mater.* **2021**, *3*, 2402–2410; d) F. Tao, Y. Zhang, K. Yin, S. Cao, X. Chang, Y. Lei, D. S. Wang, R. Fan, L. Dong, Y. Yin, X. Chen, *ACS Appl. Mater. Interfaces* **2018**, *10*, 35154–35163.
[11] a) I. Zada, W. Zhang, P. Sun, M. Imtiaz, N. Iqbal, U. Ghani, R. Naz, Y. Zhang, Y. Li, J. Gu, Q. Liu, D. Pantelić, B. Jelenković, D. Zhang, *Appl. Mater. Today* **2020**, *20*, 100669; b) S. Kim, Z. Tahir, M. U. Rashid, J. I. Jang, Y. S. Kim, *ACS Appl. Mater. Interfaces* **2021**; c) L. Song, X.-F. Zhang, Z. Wang, T. Zheng, J. Yao, *Desalination* **2021**, *507*, 115024.
[12] a) Z. Zhu, P. Mu, Y. Fan, W. Bai, Z. Zhang, H. Sun, W. Liang, A. Li, *Eur. Polym. J.* **2020**, *126*, 109560; b) L. Zong, M. Li, C. Li, *Nano Energy* **2018**, *50*, 308–315.
[13] a) W. Li, X. Tian, X. Li, S. Han, C. Li, X.-Z. Zhai, Y. Kang, Z.-Z. Yu, *J. Mater. Chem. A* **2021**, *9*, 14859–14867; b) Y. Wang, C. Wang, X. Song, S. K. Megarajan, H. Jiang, *J. Mater. Chem. A* **2018**, *6*, 963–971; c) X. Liu, D. D.

Mishra, Y. Li, L. Gao, H. Peng, L. Zhang, C. Hu, *ACS Sustainable Chem. Eng.* **2021**, *9*, 4571–4582.
[14] a) H. Ghasemi, G. Ni, A. M. Marconnet, J. Loomis, S. Yerci, N. Miljkovic, G. Chen, *Nat. Commun.* **2014**, *5*, 4449; b) W. Shang, T. Deng, *Nat. Energy* **2016**, *1*, 16133.
[15] a) F. Zhao, Y. Guo, X. Zhou, W. Shi, G. Yu, *Nat. Rev. Mater.* **2020**, *5*, 388–401; b) T. Yang, H. Lin, K.-T. Lin, B. Jia, *Sustain. Mater. Technol.* **2020**, *25*, e00182.
[16] a) X. Luo, J. Shi, C. Zhao, Z. Luo, X. Gu, H. Bao, *Appl. Energy* **2021**, *302*, 117581; b) P. Tao, G. Ni, C. Song, W. Shang, J. Wu, J. Zhu, G. Chen, T. Deng, *Nat. Energy* **2018**, *3*, 1031–1041.
[17] a) M. Gao, L. Zhu, C. K. Peh, G. W. Ho, *Energy Environ. Sci.* **2019**, *12*, 841–864; b) X. Wu, G. Y. Chen, G. Owens, D. Chu, H. Xu, *Mater. Today Energy* **2019**, *12*, 277–296; c) M. S. Irshad, N. Arshad, X. Wang, *Global Challenges* **2021**, *5*, 2000055.
[18] a) S. C. Fu, X. L. Zhong, Y. Zhang, T. W. Lai, K. C. Chan, K. Y. Lee, C. Y. H. Chao, *Energy Build.* **2020**, *225*, 110313; b) H. Ren, M. Tang, B. Guan, K. Wang, J. Yang, F. Wang, M. Wang, J. Shan, Z. Chen, D. Wei, H. Peng, Z. Liu, *Adv. Mater.* **2017**, *29*, 1702590.
[19] a) X. Wang, Y. He, X. Liu, J. Zhu, *Powder Technol.* **2017**, *321*, 276–285; b) X. Wang, Y. He, X. Liu, G. Cheng, J. Zhu, *Appl. Energy* **2017**, *195*, 414–425; c) I. Ibrahim, D. H. Seo, A. M. McDonagh, H. K. Shon, L. Tijing, *Desalination* **2021**, *500*, 114853; d) J. Zhou, Y. Gu, P. Liu, P. Wang, L. Miao, J. Liu, A. Wei, X. Mu, J. Li, J. Zhu, *Adv. Funct. Mater.* **2019**, *29*, 1903255; e) W. Guan, Y. Guo, G. Yu, *Small* **2021**, *17*, 2007176.
[20] C. Fei Guo, T. Sun, F. Cao, Q. Liu, Z. Ren, *Light-Sci. Appl.* **2014**, *3*, e161–e161.
[21] a) J. Yao, Z. Zheng, G. Yang, *Nanoscale* **2018**, *10*, 2876–2886; b) C. K. Carniglia, D. G. Jensen, *Appl. Opt.* **2002**, *41*, 3167–3171; c) P. K. Chatterjee, S. D. S. Malhi, M. deWit, H. Hosack, M. G. Harward, M. M. Moslehi, H. Hosack, in *Reference Data for Engineers (Ninth Edition)* (Eds.: W. M. Middleton, M. E. Van Valkenburg), Newnes, Woburn, **2002**, pp. 20–21-20-113; d) J. Wang, R. Shi, W. Wang, N. Cai, P. Chen, D. Kong, A. Amini, C. Cheng, *Sci. Rep.* **2018**, *8*, 12283; e) J. Rodríguez-Fernández, A. M. Funston, J. Pérez-Juste, R. A. Álvarez-Puebla, L. M. Liz-Marzán, P. Mulvaney, *Phys. Chem. Chem. Phys.* **2009**, *11*, 5909–5914; f) A. Larena, F. Millán, G. Perez, G. Pinto, *Appl. Surf. Sci.* **2002**, *187*, 339–346; g) A. B. Murphy, *Sol. Energy Mater. Sol. Cells* **2007**, *91*, 1326–1337; h) Y. Guo, F. Zhao, X. Zhou, Z. Chen, G. Yu, *Nano Lett.* **2019**, *19*, 2530–2536.
[22] a) E. Petryayeva, U. J. Krull, *Anal. Chim. Acta* **2011**, *706*, 8–24; b) M. Ding, D. Chen, in *Nanoarchitectonics for Smart Delivery and Drug Targeting* (Eds.: A. M. Holban, A. M. Grumezescu), William Andrew Publishing, **2016**, pp. 227–260.
[23] a) Z. Zalevsky, I. Abdulhalim, in *Integrated Nanophotonic Devices (Second Edition)* (Eds.: Z. Zalevsky, I. Abdulhalim), William Andrew Publishing, Oxford, **2014**, pp. 179–245; b) K. H. Hwang, S. H. Jeon, J. S. Lee, G. H. Lee, Y. S. Jeong, P. Claesson, S. H. Yun, J. H. Boo, in *Encyclopedia of Interfacial Chemistry* (Ed.: K. Wandelt), Elsevier, Oxford, **2018**, pp. 460–464; c) M. Peixoto de Almeida, E. Pereira, P. Baptista, I. Gomes, S. Figueiredo, L. Soares, R. Franco, in *Comprehensive Analytical Chemistry, Vol. 66* (Eds.: M. Valcárcel, Á. I. López-Lorente), Elsevier, **2014**, pp. 529–567; d) K. K. Paul, P. K. Giri, in *Encyclopedia of Interfacial Chemistry* (Ed.: K. Wandelt), Elsevier, Oxford, **2018**, pp. 786–794; e) T. P. Araujo, J. Quiroz, E. C. M. Barbosa, P. H. C. Camargo, *Curr. Opin. Colloid Interface Sci.* **2019**, *39*, 110–122; f) I. Ibrahim, V. Bhoopal, D. H. Seo, M. Afsari, H. K. Shon, L. D. Tijing, *Mater. Today Energy* **2021**, *21*, 100716.
[24] C. Zhang, H.-Q. Liang, Z.-K. Xu, Z. Wang, *Adv. Sci.* **2019**, *6*, 1900883.
[25] a) O. Bait, *Sustain. Energy Technol. Assess.* **2020**, *37*, 100597; b) A. Raza, J.-Y. Lu, S. Alzaim, H. Li, T. Zhang, *Energies* **2018**, *11*, 253; c) J. Liang, H. Liu, J. Yu, L. Zhou, J. Zhu, *Nat. Photonics* **2019**, *8*, 771–786.
[26] a) C. Song, L. Wang, X. Li, L. Guo, Y. Leng, X. Jin, L. Ye, *Inorg. Chem. Commun.* **2021**, *133*, 108886; b) D. Zhang, Y. Cai, Q. Liang, Z. Wu, N. Sheng, M. Zhang, B. Wang, S. Chen, *ACS Sustainable Chem. Eng.* **2020**, *8*, 9017–9026; c) I. Ibrahim, D. H. Seo, A. Angeloski, A. McDonagh, H. K. Shon, L. D. Tijing, *Sol. Energy Mater. Sol. Cells* **2021**, *232*, 111377.
[27] D. Guo, X. Yang, *Sci. China Mater.* **2019**, *62*, 711–718.
[28] J. Li, D. Chu, in *Multifunctional Photocatalytic Materials for Energy* (Eds.: Z. Lin, M. Ye, M. Wang), Woodhead Publishing, **2018**, pp. 49–78.
[29] a) D. Yang, D. Ma, *Adv. Opt. Mater.* **2019**, *7*, 1800522; b) D. Zhu, Q. Zhou, *Environ. Nanotechnol., Monit. Manage.* **2019**, *12*, 100255; c) M. Tschurl, in *Encyclopedia of Interfacial Chemistry* (Ed.: K. Wandelt), Elsevier, Oxford, **2018**, pp. 573–580; d) W. W. Gärtner, *Phys. Rev.* **1961**, *122*, 419–424; e) L. T. Contreras Montoya, S. Lain, M. Issa, A. Ilinca, in *Hybrid Renewable Energy Systems and Microgrids* (Ed.: E. Kabalci), Academic Press, **2021**, pp. 103–177.
[30] L.-C. Tien, C.-H. Ho, in *Gallium Oxide* (Eds.: S. Pearton, F. Ren, M. Mastro), Elsevier, **2019**, pp. 67–90.
[31] a) F. P. Kinik, S. Kampouri, F. M. Ebrahim, B. Valizadeh, K. C. Stylianou, in *Comprehensive Coordination Chemistry III* (Eds.: E. C. Constable, G. Parkin, L. Que Jr), Elsevier, Oxford, **2021**, pp. 590–616; b) J. Wu, W. Walukiewicz, W. Shan, K. M. Yu, J. W. Ager, E. E. Haller, H. Lu, W. J. Schaff, *Phys. Rev. B* **2002**, *66*, 201403.
[32] A. Agrawal, S. H. Cho, O. Zandi, S. Ghosh, R. W. Johns, D. J. Milliron, *Chem. Rev.* **2018**, *118*, 3121–3207.
[33] a) P. R. Chalker, *Thin Solid Films* **1999**, *343–344*, 616–622; b) J. Zhang, M. Zhang, S. Lin, X. Fu, X. Wang, *J. Catal.* **2014**, *310*, 24–30.
[34] a) S. Kurian, H. Seo, H. Jeon, *J. Phys. Chem. C.* **2013**, *117*, 16811–16819; b) X. Zhang, L. Zhang, *J. Phys. Chem. C.* **2010**, *114*, 18198–18206.
[35] a) M. Tang, J. Shang, Y. Zhang, *RSC Adv.* **2018**, *8*, 640–646; b) J. Wang, Z. Wang, B. Huang, Y. Ma, Y. Liu, X. Qin, X. Zhang, Y. Dai, *ACS Appl. Mater. Interfaces* **2012**, *4*, 4024–4030.
[36] a) J. Jang, H. Kim, J. S. Lee, *Catal. Today* **2012**, *185*, 270–277; b) K. Afroz, M. Moniruddin, N. Bakranov, S. Kudaibergenov, N. Nuraje, *J. Mater. Chem. A* **2018**, *6*, 21696–21718; c) J. Piprek, in *Semiconductor Optoelectronic Devices* (Ed.: J. Piprek), Academic Press, Boston, **2003**, pp. 49–82.
[37] D. Sinha, D. De, A. Ayaz, *Spectrochim. Acta Part A* **2018**, *193*, 467–474.
[38] A. Yarahmadi, S. Sharifnia, *Dyes Pigm.* **2014**, *107*, 140–145.
[39] a) N. Wu, *Nanoscale* **2018**, *10*, 2679–2696; b) M. Valenti, M. P. Jonsson, G. Biskos, A. Schmidt-Ott, W. A. Smith, *J. Mater. Chem. A* **2016**, *4*, 17891–17912.
[40] D. C. Ratchford, A. D. Dunkelberger, I. Vurgaftman, J. C. Owrutsky, P. E. Pehson, *Nano Lett.* **2017**, *17*, 6047–6055.
[41] a) A. Peter Amalathas, M. M. Alkaisi, *Micromachines* **2019**, *10*, 619; b) F. J. Beck, A. Polman, K. R. Catchpole, *J. Appl. Phys.* **2009**, *105*, 114310.
[42] S. Morawiec, M. J. Mendes, F. Priolo, I. Crupi, *Mater. Sci. Semicond. Process.* **2019**, *92*, 10–18.
[43] X. Fan, W. Zheng, D. J. Singh, *Light-Sci. Appl.* **2014**, *3*, e179–e179.
[44] S. K. Cushing, J. Li, J. Bright, B. T. Yost, P. Zheng, A. D. Bristow, N. Wu, *J. Phys. Chem. C.* **2015**, *119*, 16239–16244.
[45] a) H. Li, Y. He, Z. Liu, B. Jiang, Y. Huang, *Energy* **2017**, *139*, 210–219; b) D. Wu, C. Zhao, Y. Xu, X. Zhang, L. Yang, Y. Zhang, Z. Gao, Y.-Y. Song, *ACS Appl. Nano Mater.* **2020**, *3*, 10895–10904.
[46] a) L. Shi, Y. He, Y. Huang, B. Jiang, *Energy Convers. Manage.* **2017**, *149*, 401–408; b) X. Zhang, L. Ren, J. Xu, B. Shang, X. Liu, W. Xu, *Small* **2022**, *18*, 2105198; c) W. Li, Y. Chen, L. Yao, X. Ren, Y. Li, L. Deng, *Desalination* **2020**, *478*, 114288.
[47] Z. Ai, Y. Zhao, R. Gao, L. Chen, T. Wen, W. Wang, T. Zhang, W. Ge, S. Song, *J. Cleaner Prod.* **2022**, *357*, 132000.
[48] W. Xia, H. Cheng, S. Zhou, N. Yu, H. Hu, *J. Colloid Interface Sci.* **2022**, *625*, 289–296.
[49] a) M. S. Vezie, S. Few, I. Meager, G. Pieridou, B. Dörling, R. S. Ashraf, A. R. Goñi, H. Bronstein, I. McCulloch, S. C. Hayes, M. Campoy-Quiles, J. Nelson, *Nat. Mater.* **2016**, *15*, 746–753; b) D. Pospiech, D. Jehnichen, C. Horn, M. Plötner, in *Fascinating Fluoropolymers and Their Applications* (Eds.: B. Ameduri, S. Fomin), Elsevier, **2020**, pp. 227–268; c) H. Peng, X. Sun, W. Weng, X. Fang, in *Polymer Materials for Energy and Electronic Applications* (Eds.: H. Peng, X. Sun, W. Weng, X. Fang), Academic Press, **2017**, pp. 9–61.
[50] a) Y. Wang, H. Zhang, Z. Wang, L. Feng, *ACS Appl. Polym. Mater.* **2020**, *2*, 4222–4240; b) G. Griffini, J. D. Douglas, C. Piliego, T. W. Holcombe, S. Turri, J. M. J. Fréchet, J. L. Mynar, *Adv. Mater.* **2011**, *23*, 1660–1664; c) Z. Zhang, M. Liao, H. Lou, Y. Hu, X. Sun, H. Peng, *Adv. Mater.* **2018**, *30*, 1704261.
[51] Y. Shi, O. Ilic, H. A. Atwater, J. R. Greer, *Nat. Commun.* **2021**, *12*, 2797.
[52] a) W. Cao, X. Zhou, N. C. McCallum, Z. Hu, Q. Z. Ni, U. Kapoor, C. M. Heil, K. S. Cay, T. Zand, A. J. Mantanona, A. Jayaraman, A. Dhinojwala, D. D. Deheyn, M. D. Shawkey, M. D. Burkart, J. D. Rinehart, N. C. Gianneschi, *J. Am. Chem. Soc.* **2021**, *143*, 2622–2637; b) C. Qi, L.-H. Fu, H. Xu, T.-F. Wang, J. Lin, P. Huang, *Sci. China Chem.* **2019**, *62*, 162–188.
[53] a) T. C. Bond, R. W. Bergstrom, *Aerosol Sci. Technol.* **2006**, *40*, 27–67; b) A. A. Balandin, *Nat. Mater.* **2011**, *10*, 569–581; c) Q. Zhang, W. Xu, X. Wang, *Sci. China Mater.* **2018**, *61*, 905; d) V.-D. Dao, H.-S. Choi, *Global Challenges* **2018**, *2*, 1700094.
[54] H. Matsubara, G. Kikugawa, T. Bessho, T. Ohara, *Diamond Relat. Mater.* **2020**, *102*, 107669.
[55] C. Liu, J. Huang, C.-E. Hsiung, Y. Tian, J. Wang, Y. Han, A. Fratalocchi, *Adv. Sustainable Syst.* **2017**, *1*, 1600013.

[56] M. Alberghini, M. Morciano, L. Bergamasco, M. Fasano, L. Lavagna, G. Humbert, E. Sani, M. Pavese, E. Chiavazzo, P. Asinari, *Sci. Rep.* **2019**, *9*, 4701.
[57] a) B. Han, Y.-L. Zhang, Q.-D. Chen, H.-B. Sun, *Adv. Funct. Mater.* **2018**, *28*, 1802235; b) Y. Wang, M. Zhang, X. Shen, H. Wang, H. Wang, K. Xia, Z. Yin, Y. Zhang, *Small* **2021**, *17*, 2008079.
[58] J. Fang, J. Liu, J. Gu, Q. Liu, W. Zhang, H. Su, D. Zhang, *Chem. Mater.* **2018**, *30*, 6217–6221.
[59] a) W. Zechang, W. Jiang, G. Shuai, T. Swee Ching, *Nano Res. Energy* **2022**, *1*, e9120014; b) Y. Liu, J. Zhao, S. Zhang, D. Li, X. Zhang, Q. Zhao, B. Xing, *Environ. Sci.-Nano* **2022**, *9*, 2264–2296; c) A. H. Elsheikh, S. W. Sharshir, M. K. Ahmed Ali, J. Shaibo, E. M. A. Edreis, T. Abdelhamid, C. Du, Z. Haiou, *Sol. Energy* **2019**, *177*, 561–575; d) S. Karami, F. Arabpour Roghabadi, M. Maleki, V. Ahmadi, S. M. Sadrameli, *Sol. Energy* **2021**, *225*, 747–772; e) R. Djellabi, L. Noureen, V.-D. Dao, D. Meroni, E. Falletta, D. D. Dionysiou, C. L. Bianchi, *Chem. Eng. J.* **2022**, *431*, 134024.
[60] a) C. Zhang, B. Yuan, Y. Liang, L. Yang, L. Bai, H. Yang, D. Wei, W. Wang, H. Chen, *Sol. Energy Mater. Sol. Cells* **2021**, *227*, 111127; b) X. Li, J. Li, J. Lu, N. Xu, C. Chen, X. Min, B. Zhu, H. Li, L. Zhou, S. Zhu, T. Zhang, J. Zhu, *Joule* **2018**, *2*, 1331–1338.
[61] S. Behera, C. Kim, K. Kim, *Langmuir* **2020**, *36*, 12494–12503.
[62] M. Wang, P. Wang, J. Zhang, C. Li, Y. Jin, *ChemSusChem* **2019**, *12*, 467–472.
[63] F. Yang, J. Chen, Z. Ye, D. Ding, N. V. Myung, Y. Yin, *Adv. Funct. Mater.* **2021**, *31*, 2006294.
[64] Y. Chen, H. Qiu, X. Li, Q. Tong, M. Jensen, Q. Li, N. Wang, *Appl. Surf. Sci.* **2022**, *582*, 152483.
[65] M. Khajevand, S. Azizian, R. Boukherroub, *ACS Appl. Mater. Interfaces* **2021**, *13*, 31680–31690.
[66] L. Hao, N. Liu, H. Bai, P. He, R. Niu, J. Gong, *J. Colloid Interface Sci.* **2022**, *608*, 840–852.
[67] L. Zang, L. Sun, S. Zhang, C. Finnerty, A. Kim, J. Ma, B. Mi, *Chem. Eng. J.* **2021**, *422*, 129998.
[68] X. N. Zhang, C. Du, Z. Wei, M. Du, Q. Zheng, Z. L. Wu, *Macromolecules* **2021**.
[69] J. Feng, B. Bai, L. Yang, N. Hu, H. Wang, *Mater. Chem. Phys.* **2021**, *271*, 124904.
[70] F. Yu, Z. Chen, Z. Guo, M. S. Irshad, L. Yu, J. Qian, T. Mei, X. Wang, *ACS Sustainable Chem. Eng.* **2020**, *8*, 7139–7149.
[71] X. Chen, Z. Wu, D. Lai, M. Zheng, L. Xu, J. Huo, Z. Chen, B. Yuan, M.-L. Fu, *J. Mater. Chem. A* **2020**, *8*, 22645–22656.
[72] H. Zhang, L. Li, B. Jiang, Q. Zhang, J. Ma, D. Tang, Y. Song, *ACS Appl. Mater. Interfaces* **2020**, *12*, 16503–16511.
[73] M. Zhu, J. Yu, C. Ma, C. Zhang, D. Wu, H. Zhu, *Sol. Energy Mater. Sol. Cells* **2019**, *191*, 83–90.
[74] F. Wang, D. Wei, Y. Li, T. Chen, P. Mu, H. Sun, Z. Zhu, W. Liang, A. Li, *J. Mater. Chem. A* **2019**, *7*, 18311–18317.
[75] J. Liu, H. Yang, K. Liu, R. Miao, Y. Fang, *ChemSusChem* **2020**, *13*, 749–755.
[76] Z. Wang, Y. Yan, X. Shen, Q. Sun, C. Jin, *Sustain. Energy Fuels* **2020**, *4*, 354–361.
[77] X. Zhou, F. Zhao, Y. Guo, Y. Zhang, G. Yu, *Energy Environ. Sci.* **2018**, *11*, 1985–1992.
[78] Z. Lin, T. Wu, B. Jia, J. Shi, B. Zhou, C. Zhu, Y. Wang, R. Liang, M. Mizuno, *Colloids Surf. A* **2022**, *637*, 128272.
[79] Z. Huang, Y.-H. Luo, W.-Y. Geng, Y. Wan, S. Li, C.-S. Lee, *Small Methods* **2021**, *5*, 2100036.
[80] T. Xu, Y. Xu, J. Wang, H. Lu, W. Liu, J. Wang, *Chem. Eng. J.* **2021**, *415*, 128893.
[81] Z. Xu, X. Ran, D. Wang, M. Zhong, Z. Zhang, *Desalination* **2022**, *525*, 115495.
[82] J. Chen, B. Li, G. Hu, R. Aleisa, S. Lei, F. Yang, D. Liu, F. Lyu, M. Wang, X. Ge, F. Qian, Q. Zhang, Y. Yin, *Nano Lett.* **2020**, *20*, 6051–6058.
[83] F. Wang, Y. Su, Y. Li, D. Wei, H. Sun, Z. Zhu, W. Liang, A. Li, *ACS Appl. Energ. Mater.* **2020**, *3*, 8746–8754.
[84] C. Zhang, P. Xiao, F. Ni, L. Yan, Q. Liu, D. Zhang, J. Gu, W. Wang, T. Chen, *ACS Sustainable Chem. Eng.* **2020**, *8*, 5328–5337.
[85] X. Zhou, F. Zhao, Y. Guo, B. Rosenberger, G. Yu, *Sci. Adv.* **2019**, *5*, eaaw5484.
[86] J. He, G. Zhao, P. Mu, H. Wei, Y. Su, H. Sun, Z. Zhu, W. Liang, A. Li, *Sol. Energy Mater. Sol. Cells* **2019**, *201*, 110111.
[87] Y. Fan, W. Bai, P. Mu, Y. Su, Z. Zhu, H. Sun, W. Liang, A. Li, *Sol. Energy Mater. Sol. Cells* **2020**, *206*, 110347.
[88] D. Hao, Y. Yang, B. Xu, Z. Cai, *Appl. Therm. Eng.* **2018**, *141*, 406–412.
[89] R. Zhu, D. Wang, J. Zhang, Z. Yu, M. Liu, S. Fu, *Desalination* **2022**, *527*, 115585.
[90] B. Soo Joo, I. Soo Kim, I. Ki Han, H. Ko, J. Gu Kang, G. Kang, *Appl. Surf. Sci.* **2022**, *583*, 152563.
[91] H. Lim, M. Kim, J. Yoo, D. Lee, M. Lee, B. Na, S. K. Kim, *Desalination* **2022**, *524*, 115477.
[92] Y. Liu, J. Xiong, A. Li, R. Wang, L. Wang, X. Qin, *Text. Res. J.* **2021**, *91*, 2624–2634.
[93] F. He, M. Han, J. Zhang, Z. Wang, X. Wu, Y. Zhou, L. Jiang, S. Peng, Y. Li, *Nano Energy* **2020**, *71*, 104650.
[94] Z. Xu, N. Rao, C.-Y. Tang, W.-C. Law, *Micromachines* **2020**, *11*, 867.
[95] Z. Li, M. Zheng, N. Wei, Y. Lin, W. Chu, R. Xu, H. Wang, J. Tian, H. Cui, *Sol. Energy Mater. Sol. Cells* **2020**, *205*, 110254.
[96] Y. Yang, H. Zhao, Z. Yin, J. Zhao, X. Yin, N. Li, D. Yin, Y. Li, B. Lei, Y. Du, W. Que, *Mater. Horiz.* **2018**, *5*, 1143–1150.
[97] F. Tao, Y. Zhang, K. Yin, S. Cao, X. Chang, Y. Lei, D. Wang, R. Fan, L. Dong, Y. Yin, X. Chen, *Sustain. Energy Fuels* **2018**, *2*, 2762–2769.
[98] H. Liu, X. Zhang, Z. Hong, Z. Pu, Q. Yao, J. Shi, G. Yang, B. Mi, B. Yang, X. Liu, H. Jiang, X. Hu, *Nano Energy* **2017**, *42*, 115–121.
[99] A. S. Alketbi, A. Raza, M. Sajjad, H. Li, F. AlMarzooqi, T. Zhang, *EcoMat* **2022**, *4*, e12157.
[100] M. S. Irshad, X. Wang, M. S. Abbasi, N. Arshad, Z. Chen, Z. Guo, L. Yu, J. Qian, J. You, T. Mei, *ACS Sustainable Chem. Eng.* **2021**, *9*, 3887–3900.
[101] X. Wang, Z. Li, Y. Wu, H. Guo, X. Zhang, Y. Yang, H. Mu, J. Duan, *ACS Appl. Mater. Interfaces* **2021**, *13*, 10902–10915.
[102] P. Ying, M. Li, F. Yu, Y. Geng, L. Zhang, J. He, Y. Zheng, R. Chen, *ACS Appl. Mater. Interfaces* **2020**, *12*, 32880–32887.
[103] Y. Zhang, F. Tao, S. Cao, K. Yin, X. Chang, R. Fan, C. Fan, L. Dong, Y. Yin, X. Chen, *Sol. Energy Mater. Sol. Cells* **2019**, *200*, 110043.
[104] X. Song, H. Song, N. Xu, H. Yang, L. Zhou, L. Yu, J. Zhu, J. Xu, K. Chen, *J. Mater. Chem. A* **2018**, *6*, 22976–22986.
[105] J. Wang, Y. Li, L. Deng, N. Wei, Y. Weng, S. Dong, D. Qi, J. Qiu, X. Chen, T. Wu, *Adv. Mater.* **2017**, *29*, 1603730.
[106] Y. Guo, J. Bae, Z. Fang, P. Li, F. Zhao, G. Yu, *Chem. Rev.* **2020**, *120*, 7642–7707.
[107] a) H.-H. Huang, R. K. Joshi, K. K. H. De Silva, R. Badam, M. Yoshimura, *J. Membr. Sci.* **2019**, *572*, 12–19; b) X. Zhou, Y. Guo, F. Zhao, G. Yu, *Acc. Chem. Res.* **2019**, *52*, 3244–3253.
[108] a) X. F. Huang, L. Q. Pan, C. X. Li, Q. Wang, G. Sun, K. Lu, *Wuli Xuebao/ Acta Phys. Sin.* **2012**, *61*; b) Q. Hu, H. Zhao, S. Ouyang, *Phys. Chem. Chem. Phys.* **2017**, *19*, 21540–21547.
[109] a) H. Yao, B. D. Olsen, *Soft Matter* **2021**, *17*, 5303–5318; b) Y. Liu, X. Liu, B. Duan, Z. Yu, T. Cheng, L. Yu, L. Liu, K. Liu, *J. Phys. Chem. Lett.* **2021**, *12*, 2587–2592.
[110] a) A. Penlidis, E. Vivaldo-Lima, J. C. Hernández-Ortiz, E. Saldívar-Guerra, in *Handbook of Polymer Synthesis, Characterization, and Processing*, John Wiley & Sons, Inc, Hoboken, NJ, USA, **2013**, pp. 249–271; b) R. P. Wool, in *Bio-Based Polymers and Composites* (Eds.: R. P. Wool, X. S. Sun), Academic Press, Burlington, **2005**, pp. 202–255.
[111] M. S. Rahaman, S. M. M. Hasnine, T. Ahmed, S. Sultana, M. A. Q. Bhuiyan, M. S. Manir, N. Ullah, S. K. Sen, M. N. Hossain, M. S. Hossain, N. C. Dafader, *Iran. Polym. J.* **2021**.
[112] Y. Wu, S. Joseph, N. R. Aluru, *J. Phys. Chem. B* **2009**, *113*, 3512–3520.
[113] a) K.-P. Wang, Y. Yang, Q. Zhang, Z. Xiao, L. Zong, T. Ichitsubo, L. Wang, *Mater. Chem. Front.* **2021**, *5*, 5106–5114; b) G. Chen, T. Li, C. Chen, W. Kong, M. Jiao, B. Jiang, Q. Xia, Z. Liang, Y. Liu, S. He, L. Hu, *ACS Nano* **2021**, *15*, 11244–11252.
[114] P. Lin, S. Ma, X. Wang, F. Zhou, *Adv. Mater.* **2015**, *27*, 2054–2059.
[115] X. Wang, Q. Zhang, *Powder Technol.* **2020**, *371*, 55–63.
[116] M.-H. Zhao, X.-P. Chen, Q. Wang, *Sci. Rep.* **2014**, *4*, 5376.
[117] Z. Liu, H. Song, D. Ji, C. Li, A. Cheney, Y. Liu, N. Zhang, X. Zeng, B. Chen, J. Gao, Y. Li, X. Liu, D. Aga, S. Jiang, Z. Yu, Q. Gan, *Global Challenges* **2017**, *1*, 1600003.
[118] X. Song, H. Song, S. Wang, J. Liu, L. Zhou, J. Xu, K. Chen, *J. Mater. Chem. A* **2019**, *7*, 26496–26503.
[119] A. Vasilev, T. Lorenz, C. Breitkopf, *Polymer* **2021**, *13*, 315.
[120] S. Engelmann, J. Meyer, R. Hentschke, *Phys. Rev. B* **2017**, *96*.
[121] B. Ni, T. Watanabe, S. R. Phillpot, *J. Phys. Condens. Matter* **2009**, *21*, 084219.
[122] V. Rashidi, E. J. Coyle, K. Sebeck, J. Kieffer, K. P. Pipe, *J. Phys. Chem. B* **2017**, *121*, 4600–4609.
[123] T. A. Cooper, S. H. Zandavi, G. W. Ni, Y. Tsurimaki, Y. Huang, S. V. Boriskina, G. Chen, *Nat. Commun.* **2018**, *9*, 5086.

[124] a) P. Mohazzab, *J. Appl. Math. Phys.* **2017**, *Vol.05No.04*, 9; b) N.-w. Li, C.-p. Ho, K.-l. Yick, J.-y. Zhou, *Res. J. Text. Apparel* **2020**, *24*, 147–161; c) P. G. Ryan, *Environ. Res. Lett.* **2015**, *10*, 084019.
[125] S. Sornkamnerd, M. K. Okajima, T. Kaneko, *ACS Omega* **2017**, *2*, 5304–5314.
[126] J. He, Y. Fan, C. Xiao, F. Liu, H. Sun, Z. Zhu, W. Liang, A. Li, *Compos. Sci. Technol.* **2021**, *204*, 108633.
[127] S. D. Janssens, V. Chaurasia, E. Fried, *J. Fluid Mech.* **2017**, *830*, 369–386.
[128] a) B. W. Chieng, N. A. Ibrahim, N. Ahmad Daud, Z. A. Talib, in *Synthesis, Technology and Applications of Carbon Nanomaterials* (Eds.: S. A. Rashid, R. N. I. Raja Othman, M. Z. Hussein), Elsevier, **2019**, pp. 177–203; b) K. Song, J. Lee, S.-O. Choi, J. Kim, *Polymers (Basel).* **2019**, *11*, 498; c) M. R. Rahimpour, M. A. Esmaeilbeig, in *Current Trends and Future Developments on (Bio-) Membranes* (Eds.: A. Basile, E. Curcio, Inamuddin), Elsevier, **2019**, pp. 143–174.
[129] a) J.-L. Liu, X.-Q. Feng, G.-F. Wang, *Phys. Rev. E Stat. Nonlin. Soft Matter Phys.* **2007**, *76*, 066103–066103; b) E. Bormashenko, *J. Colloid Interface Sci.* **2016**, *463*, 8–12.
[130] C. Suzuki, Y. Takaku, H. Suzuki, D. Ishii, T. Shimozawa, S. Nomura, M. Shimomura, T. Hariyama, *Commun. Biol.* **2021**, *4*, 708.
[131] a) Y. Yonemoto, I. Tomimitsu, K. Shimizu, T. Kunugi, *Int. J. Multiphase Flow* **2021**, *137*, 103569; b) T. L. Liu, C.-J. C. Kim, *Sci. Rep.* **2017**, *7*, 740.
[132] D. Wang, Z. Hu, G. Peng, Y. Yin, *Nanomaterials* **2021**, *11*, 686.
[133] a) N. Pal, K. Babu, A. Mandal, *J. Pet. Sci. Eng.* **2016**, *146*, 591–600; b) T. Stoebe, Z. Lin, R. M. Hill, M. D. Ward, H. T. Davis, *Langmuir* **1996**, *12*, 337–344; c) Z. Cai, Y. Gong, W. Liu, J. Fu, S. E. O'Reilly, X. Hao, D. Zhao, *Mar. Pollut. Bull.* **2016**, *109*, 49–54.
[134] a) O. World Health, **2003**; b) O. World Health, World Health Organization, Geneva, **2011**; c) S. Z. Mohd Nani, F. A. A. Majid, A. B. Jaafar, A. Mahdzir, M. N. Musa, *Evid.-Based Complement. Altern. Med.* **2016**, *2016*, 6520475–6520475.
[135] a) G. Liu, T. Chen, J. Xu, G. Yao, J. Xie, Y. Cheng, Z. Miao, K. Wang, *Cell Rep. Phys. Sci.* **2021**, *2*, 100310; b) F. Nawaz, Y. Yang, S. Zhao, M. Sheng, C. Pan, W. Que, *J. Mater. Chem. A* **2021**, *9*, 16233–16254.
[136] M. Sheng, Y. Yang, X. Bin, S. Zhao, C. Pan, F. Nawaz, W. Que, *Nano Energy* **2021**, 106468.
[137] Y. Wang, X. Wu, T. Gao, Y. Lu, X. Yang, G. Y. Chen, G. Owens, H. Xu, *Nano Energy* **2021**, *79*, 105477.
[138] J. He, Z. Zhang, C. Xiao, F. Liu, H. Sun, Z. Zhu, W. Liang, A. Li, *ACS Appl. Mater. Interfaces* **2020**, *12*, 16308–16318.
[139] Q. Xiao, Y. Zhu, Y. Xi, X. Kong, X. Ye, Z. Zhang, C. Qiu, W. Xu, S. Cheng, J. Zhang, M. Jia, E. Sun, H. Lin, J. Wang, *Chem. Eng. J.* **2022**, *430*, 133019.
[140] D. A. Kospa, A. I. Ahmed, S. E. Samra, S. A. El-Hakam, A. A. Ibrahim, *Desalination* **2022**, *528*, 115612.
[141] N. Xu, J. Li, Y. Wang, C. Fang, X. Li, Y. Wang, L. Zhou, B. Zhu, Z. Wu, S. Zhu, J. Zhu, *Sci. Adv.* **2019**, *5*, eaaw7013-eaaw7013.
[142] X. Wu, Y. Wang, P. Wu, J. Zhao, Y. Lu, X. Yang, H. Xu, *Adv. Funct. Mater.* **2021**, *31*, 2102618.
[143] Z.-C. Xiong, Y.-J. Zhu, D.-D. Qin, R.-L. Yang, *ACS Appl. Mater. Interfaces* **2020**, *12*, 32556–32565.
[144] a) H. Frank, K. E. Fussmann, E. Rahav, E. Bar Zeev, *Water Res.* **2019**, *151*, 478–487; b) A. Panagopoulos, K.-J. Haralambous, *Mar. Pollut. Bull.* **2020**, *161*, 111773.
[145] A. Karbalaei, R. Kumar, H. J. Cho, *Micromachines* **2016**, *7*, 13.
[146] Z. Huang, J. Wei, Y. Wan, P. Li, J. Yu, J. Dong, S. Wang, S. Li, C.-S. Lee, *Small* **2021**, *17*, 2101487.
[147] L. Wu, Z. Dong, Z. Cai, T. Ganapathy, N. X. Fang, C. Li, C. Yu, Y. Zhang, Y. Song, *Nat. Commun.* **2020**, *11*, 521.
[148] J. Li, X. Zhou, J. Zhang, C. Liu, F. Wang, Y. Zhao, H. Sun, Z. Zhu, W. Liang, A. Li, *ACS Appl. Energ. Mater.* **2020**, *3*, 3024–3032.
[149] a) G. N. Ngweme, D. M. M. Al Salah, A. Laffite, P. Sivalingam, D. Grandjean, J. N. Konde, C. K. Mulaji, F. Breider, J. Poté, *Sci. Total Environ.* **2021**, *754*, 142175; b) M. Fakruddin, K. S. B. Mannan, S. Andrews, *ISRN Microbiol* **2013**, *2013*, 703813–703813; c) T. Wu, G. Zhu, M. Zhu, H. Xu, J. Yang, X. Zhao, *Environ. Pollut.* **2021**, *288*, 117683; d) A. Fallahi, F. Rezvani, H. Asgharnejad, E. Khorshidi Nazloo, N. Hajinajaf, B. Higgins, *Chemosphere* **2021**, *272*, 129878.
[150] a) A. M. Gorito, J. F. J. R. Pesqueira, N. F. F. Moreira, A. R. Ribeiro, M. F. R. Pereira, O. C. Nunes, C. M. R. Almeida, A. M. T. Silva, *J. Environ. Chem. Eng.* **2021**, *9*, 105315; b) P. R. Rout, M. K. Shahid, R. R. Dash, P. Bhunia, D. Liu, S. Varjani, T. C. Zhang, R. Y. Surampalli, *J. Environ. Manage.* **2021**, *296*, 113246; c) P. Soler, L. Moreno-Mesonero, A. Zornoza, V. J. Macián, Y. Moreno, *Sci. Total Environ.* **2021**, *797*, 149070.
[151] S.-W. Nam, B.-I. Jo, Y. Yoon, K.-D. Zoh, *Chemosphere* **2014**, *95*, 156–165.
[152] L. Guo, K. Wan, J. Zhu, C. Ye, K. Chabi, X. Yu, *J. Hazard. Mater.* **2021**, *406*, 124335.
[153] L. Zhu, X. Shuai, L. Xu, Y. Sun, Z. Lin, Z. Zhou, L. Meng, H. Chen, *J. Hazard. Mater.* **2022**, *423*, 127228.
[154] a) D. Ayodhya, G. Veerabhadram, *Mater. Today Energy* **2018**, *9*, 83–113; b) J. Ma, Y. Xu, F. Sun, X. Chen, W. Wang, *EcoMat* **2021**, *3*, e12147.
[155] Q. Zhao, C. Du, Y. Jia, J. Yuan, G. Song, X. Zhou, S. Sun, C. Zhou, L. Zhao, S. Yang, *Chem. Eng. J.* **2020**, *387*, 124131.
[156] a) X. Wang, C. Sha, W. Wang, Y. Chen, Y. Yu, D. Fan, *Mater. Res. Express* **2019**, *6*, 125613; b) D. Qi, Y. Liu, Y. Liu, Z. Liu, Y. Luo, H. Xu, X. Zhou, J. Zhang, H. Yang, W. Wang, X. Chen, *Adv. Mater.* **2020**, *32*, 2004401.
[157] C. Song, D. Qi, Y. Han, Y. Xu, H. Xu, S. You, W. Wang, C. Wang, Y. Wei, J. Ma, *Environ. Sci. Technol.* **2020**, *54*, 9025–9033.
[158] J. M. Slauch, *Mol. Microbiol.* **2011**, *80*, 580–583.
[159] Y. Guo, C. M. Dundas, X. Zhou, K. P. Johnston, G. Yu, *Adv. Mater.* **2021**, *33*, 2102994.
[160] a) Y. Feng, Q. Chen, Q. Yin, G. Pan, Z. Tu, L. Liu, *ACS Appl. Bio Mater.* **2019**, *2*, 747–756; b) K. Prasad, G. S. Lekshmi, K. Ostrikov, V. Lussini, J. Blinco, M. Mohandas, K. Vasilev, S. Bottle, K. Bazaka, K. Ostrikov, *Sci. Rep.* **2017**, *7*, 1591.
[161] A. Ebrahimi, E. K. Goharshadi, M. Mohammadi, *Mater. Chem. Phys.* **2022**, *275*, 125258.
[162] Y. Xu, B. Lv, Y. Yang, X. Fan, Y. Yu, C. Song, Y. Liu, *Desalination* **2021**, *517*, 115260.
[163] M. Arvaniti, P. N. Skandamis, *Curr. Opin. Food Sci.* **2022**, *44*, 100808.
[164] a) D. Yang, Y. Wang, L. Zhao, L. Rao, X. Liao, *Food Res. Int.* **2022**, *151*, 110895; b) J. J. Alvear-Daza, A. García-Barco, P. Osorio-Vargas, H. M. Gutiérrez-Zapata, J. Sanabria, J. A. Rengifo-Herrera, *Water Res.* **2021**, *188*, 116499; c) M. Shao, C. Ye, T. Li, J. Gan, X. Yu, L. Wang, *J. Environ. Sci.* **2022**.
[165] C. Ye, Y. Chen, L. Feng, K. Wan, J. Li, M. Feng, X. Yu, *Front. Environ. Sci. Eng.* **2021**, *16*, 100.
[166] P. Sun, W. Zhang, I. Zada, Y. Zhang, J. Gu, Q. Liu, H. Su, D. Pantelić, B. Jelenković, D. Zhang, *ACS Appl. Mater. Interfaces* **2020**, *12*, 2171–2179.
[167] H. Sun, Y. Li, J. Li, Z. Zhu, W. Zhang, W. Liang, C. Ma, A. Li, *ACS Appl. Mater. Interfaces* **2021**, *13*, 33427–33436.
[168] Y. Li, X. Jin, Y. Zheng, W. Li, F. Zheng, W. Wang, T. Lin, Z. Zhu, *ACS Appl. Mater. Interfaces* **2019**, *11*, 46938–46946.
[169] a) C. Sheng, N. Yang, Y. Yan, X. Shen, C. Jin, Z. Wang, Q. Sun, *Appl. Therm. Eng.* **2020**, *167*, 114712; b) Z. Huang, S. Li, X. Cui, Y. Wan, Y. Xiao, S. Tian, H. Wang, X. Li, Q. Zhao, C.-S. Lee, *J. Mater. Chem. A* **2020**, *8*, 10742–10746; c) E. Bellos, C. Tzivanidis, *Sustain. Energy Technol. Assess.* **2018**, *28*, 22–29; d) S. Ma, C. P. Chiu, Y. Zhu, C. Y. Tang, H. Long, W. Qarony, X. Zhao, X. Zhang, W. H. Lo, Y. H. Tsang, *Appl. Energy* **2017**, *206*, 63–69.
[170] J. Li, X. Wang, Z. Lin, N. Xu, X. Li, J. Liang, W. Zhao, R. Lin, B. Zhu, G. Liu, L. Zhou, S. Zhu, J. Zhu, *Joule* **2020**, *4*, 928–937.
[171] Y. Lin, W. Zhou, Y. Di, X. Zhang, L. Yang, Z. Gan, *AIP Adv.* **2019**, *9*, 055110.
[172] X. Shan, A. Zhao, Y. Lin, Y. Hu, Y. Di, C. Liu, Z. Gan, *Adv. Sustainable Syst.* **2020**, *4*, 1900153.
[173] J. Li, M. Du, G. Lv, L. Zhou, X. Li, L. Bertoluzzi, C. Liu, S. Zhu, J. Zhu, *Adv. Mater.* **2018**, *30*, 1805159.
[174] F. Liu, B. Zhao, W. Wu, H. Yang, Y. Ning, Y. Lai, R. Bradley, *Adv. Funct. Mater.* **2018**, *28*, 1803266.
[175] Z. Wang, M. Han, F. He, S. Peng, S. B. Darling, Y. Li, *Nano Energy* **2020**, *74*, 104886.
[176] H. Li, Y. He, Y. Hu, X. Wang, *ACS Appl. Mater. Interfaces* **2018**, *10*, 9362–9368.
[177] M. Yin, Y. Hsin, X. Guo, R. Zhang, X. Huang, X. Zhang, *Sci. Total Environ.* **2021**, *759*, 143546.
[178] Y. L. Wang, G. J. Li, K. C. Chan, *Sol. Energy Mater. Sol. Cells* **2020**, *218*, 110693.

Manuscript received: August 12, 2022
Revised manuscript received: September 25, 2022
Accepted manuscript online: September 26, 2022
Version of record online: November 8, 2022